Selection and kinematic properties of ν_μ charged-current inclusive events in 5×10^{19} POT of MicroBooNE data - Public Note - (MICROBOONE-NOTE-1010-PUB)

The MicroBooNE Collaboration

July 5, 2016

Abstract

This note describes a first selection of ν_μ charged-current inclusive events in the MicroBooNE detector. MicroBooNE is a 170 ton liquid-argon time projection chamber, located at surface level in the Booster Neutrino Beam at Fermilab. The detector is therefore continuously exposed to cosmic rays, which outnumber the observed neutrino interactions by almost three orders of magnitude. Hence, the selection of neutrino interactions within the cosmic background is the first step towards any neutrino physics analysis in MicroBooNE. This note describes two approaches, which successfully select ν_μ charged-current events in a fully automated way. It also outlines further necessary steps to improve the detector understanding and reconstruction, increase the selection efficiency and address systematic uncertainties, before the first neutrino-argon cross sections can be derived.

1 Introduction

MicroBooNE is a liquid argon time projection chamber (LArTPC) with an active volume of 87 tons [1]. The drift distance between the cathode, which is operated under a voltage of -70 kV, and the wire plane anode is 2.56 m. The wire plane anode consists of three planes of wires with a plane and wire spacing of 3 mm, and wires oriented at a 60° angle. The wires are gold coated stainless steel and a total of 8256 are deployed in the anode frame. Ionization electrons created by charged particles from neutrino interactions in the liquid argon drift towards the anode under the influence of the applied electric field. The electron signals collected by the wires are read out and amplified by electronics submerged in the liquid argon, before being transported to a readout system outside the detector. The arrival times and deposited charge on the wires allows a three-dimensional reconstruction of the final state particles from a neutrino interaction. A light system consisting of 32 8-inch photomultipliers (PMTs) records associated scintillation light and delivers precise timing information for triggering and reconstruction.

MicroBooNE is the first LArTPC operating in a neutrino beam while located at surface level. Since the electrons in liquid argon move rather slowly, the maximum drift time for ionization electrons to cover the entire distance between cathode and anode in a drift field of 273 V/cm is 2.3 ms [2]. During this time window, a large number of cosmic induced particles traverse the detector, which can either overlay a triggered neutrino interaction or even deposit a sufficient amount of light to trigger the readout of an event by itself. This results in about a dozen cosmic induced particle trajectories within a 2.3 ms time window [3], which need to be tagged as background during the reconstruction and selection process.

MicroBooNE started taking neutrino data from the Booster Neutrino Beam (BNB) in October 2015 and successfully showed the identification of the first neutrino events using fully automated tools [4]. Some additional challenges observed during the operation of the TPC have been various sources of partly correlated noise observed in the TPC and PMT system and a total of about 10% of unusable channels either not delivering signals or showing high noise [5]. Techniques to improve the modeling of the current detector operating conditions in simulation and to handle these issues in the reconstruction are partly implemented and continuously being improved [6, 7]. The impact on the selection of ν_μ charged-current (CC) events presented is discussed in Section 3.2.2.

This note presents the first strategies developed for the selection of a sample of ν_μ CC events and summarizes the status by the time of summer 2016. The future goal of this study is a measurement of ν_μ CC inclusive cross section on argon, as outlined in a previous MC performance study [8]. However, the importance of developing a selection for ν_μ CC events goes beyond the measurement of a ν_μ CC inclusive cross section. Within the context of this selection, the tools for defining the necessary data quality and detector stability for physics analyses are being developed, the requirements and improvements for the detector simulation and track reconstruction chain are being identified, and the methods for tagging the cosmic background are being established. The selections presented here also serve as a starting point for further selection for more specific interaction channels such as the search for CC π^0 events [9].

In Section 4 we present two different selection approaches, which were developed in parallel. Selection I is largely based on the selection developed for the MC performance study [8]. It selects ν_μ CC interactions by identifying only the neutrino-induced muon of the interaction relying only on the geometry information associated to a given reconstructed track. For sufficient cosmic rejection it requires full containment of the interaction in the TPC fiducial volume. Selection II makes use of a more complex selection procedure factorizing the sample into sub branches depending on the observed track multiplicity. For higher track multiplicities, events not fully contained can be successfully identified by using additional calorimetric information from the track reconstruction. This increases the acceptance in selection II.

The distributions resulting from both selections presented in Section 4.3 show the difference between data taken when the beam was on and that when the beam was off. The subtraction of off-beam data subtracts the background of purely cosmic events. Beam related backgrounds (neutral current (NC) events, $\bar{\nu}_\mu$ interactions, or $\nu_e/\bar{\nu}_e$ interactions) as well as mis-identified events where a cosmic is mistaken for a neutrino interaction, which triggered the readout are still included in the data. Therefore, this on-beam minus off-beam data sample can be compared to a simulation of BNB neutrino interactions overlaid with cosmic background tracks. The simulation is normalized to match the total selected events in data and therefore no conclusions on the overall normalization offset between data and simulation are drawn at this point. The errors presented are statistical only.

In order to advance from this point on towards a cross section measurement, further studies and improvements to the detector simulation and reconstruction are being developed to improve the agreement between MC and data. Several ideas to significantly increase the acceptance and selection efficiency of ν_μ CC events are currently being evaluated and will be implemented (see also Section 7). Additionally, a full understanding of systematic uncertainties arising from the beam, neutrino interaction models and the detector properties and modeling is required and currently being worked on. A first outlook on systematics is given in Section 6.

2 Data and simulation samples

2.1 Data

The data taking period for these selections ranges from February 23, 2016, to May 22, 2016 (MicroBooNE run numbers 5212 to 6356). The beginning of this dataset marks the switch to data taking utilizing the light system for triggering, which reduces the data rate by about a factor of 20. The trigger is applied in software and requires a minimum amount of light observed during the beam window of 1.6 μs length integrated over all PMTs.

Two different data streams are utilized in this note. One is the data stream delivering on-beam data, which is taken only during periods when a beam spill from the BNB is actually sent. The other data stream is the off-beam data stream, which is taken with the exact same trigger settings as the on-beam data, but during periods when no beam was received. It is used here for a data-driven measurement of cosmic background.

Good runs during this period were selected taking into account successful operation of all detector systems, detector stability in high-level parameters relevant for this analysis, beam quality, and successful processing of all subrun files. The detector stability study monitors variables related to reconstructed flashes, tracks and vertices [10]. It is required that a run was within 3-σ of the average for all relevant variables and in both data streams in order to enter the good run list. A fraction of 91.7% of the delivered protons on target (POT) from the BNB pass these criteria.

To comply with the MicroBooNE data blindness policy, the open data sample for the BNB on-beam stream is further down-sized to not exceed a total of 5×10^{19} POT. Therefore, the on-beam sample used here ends on April 17 with run 5946, which adds up to a total of 4.95×10^{19} POT [11]. For the off-beam sample, which is taken with a prescale factor of 2, the entire period is used.

This leaves 546910 on-beam events and 388471 off-beam events to be analyzed in this note. Taking into account the different run periods, trigger efficiencies and the prescaling of the streams, the off-beam stream needs to be scaled with a factor of ~ 1.23 before comparing to the on-beam sample used here.

2.2 Simulation

The software framework used for both, processing of data and generation of simulation is the LArSoft software framework [12]. The first stage in the simulation is the generator stage, where neutrino interactions are simulated using GENIE 2.8.6, and GENIE 2.10.6 (for systematics samples, see Section 6) [13] and overlaid with simulated cosmic background using CORSIKA v7.4003 [14]. The next step propagates final state particles through the detector using GEANT v4.9.6.p04d [15]. The last simulation step simulates the detector response as implemented in LArSoft v4.36.00.

The baseline simulation sample and all samples used for model systematics studies in Section 6 comprise of 200,000 neutrino interactions inside the MicroBooNE cryostat volume.

3 Reconstruction

3.1 Optical reconstruction

The light collected on MicroBooNE's 32 PMTs is used to reconstruct optical hits. Each PMT's waveform is scanned for signals which are located by first applying a rolling-baseline estimation, in order to be less sensitive to possible fluctuations in the signal baseline. At this stage a threshold-based hit-reconstruction algorithm is applied, requiring pulses of a minimum area in order for a hit to be reconstructed. Each reconstructed hit is associated with a PMT number, a time (with respect to the trigger time, in μs), and a photo-electron (PE) count. Once, for a given event, optical hits are reconstructed on all 32 PMTs, information

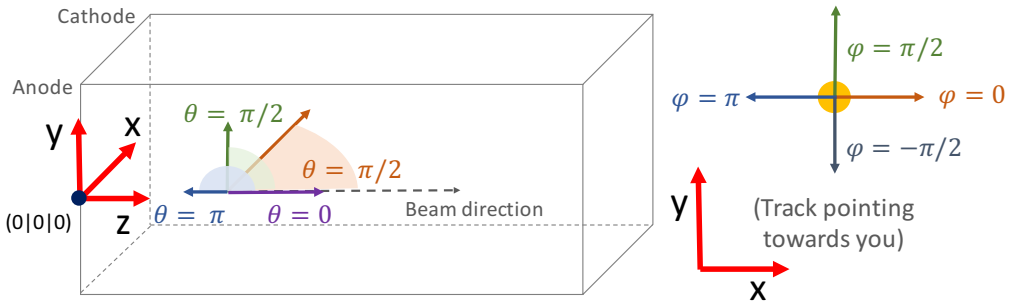

Figure 1: Definitions of the MicroBooNE coordinate system and the angles θ and ϕ. The angle θ is the angle of the track w.r.t. the beam axis. ϕ is rotating around the track.

from all PMTs is combined into optical flashes, which are meant to represent interactions in the detector, as seen by the PMT system. Flashes are reconstructed by requiring a time-coincidence of $\sim$1 μs between hits on all PMTs. The flash information further used in this note is the flash time w.r.t. the trigger time, the total amount of light seen (measured in PE and integrated over all PMTs contributing to the flash), and the PE-weighted center of the flash within the anode plane (Y and Z coordinates as shown in Figure 1).

3.2 TPC reconstruction

3.2.1 Track reconstruction chain

Figure 2 summarizes the reconstruction chain applied to the TPC data and MC in this analysis. The raw signal recorded on the wires first passes a noise filter [5], before hits are extracted from the observed waveforms on each wire. In the next step, hits that are connected in space and time are grouped into clusters. The clusters in all three planes then have to be merged between planes based on time and spatial information in order to create three-dimensional reconstructed objects.

In order to make a first attempt in removing cosmic tracks, the reconstruction chain is divided in two passes: In the cosmic pass, all objects are attempted to be reconstructed. Then, tracks that are crossing any two of the Y and Z boundaries of the TPC (called through-going) are tagged and all hits associated to these through-going tracks, are then removed. Other algorithms attempting the reconstruction of a neutrino interaction follow and are run only on the remaining hits. The three-dimensional objects used in the event selection are tracks characterized by three-dimensional end points and track lengths, and vertices, given in three-dimensional coordinates. Additionally, a calorimetric reconstruction is run on tracks that provides the energy loss per unit path length dE/dx [16].

Figure 2 shows several alternative algorithms that are run on the same data and are available for analysis. The pandora reconstruction chain is further described in [7] and is used in selection I. Selection II is based on the Projection Matching Algorithm (PMA) [17]. The performance of the tracking algorithms is further discussed in Section 3.2.3.

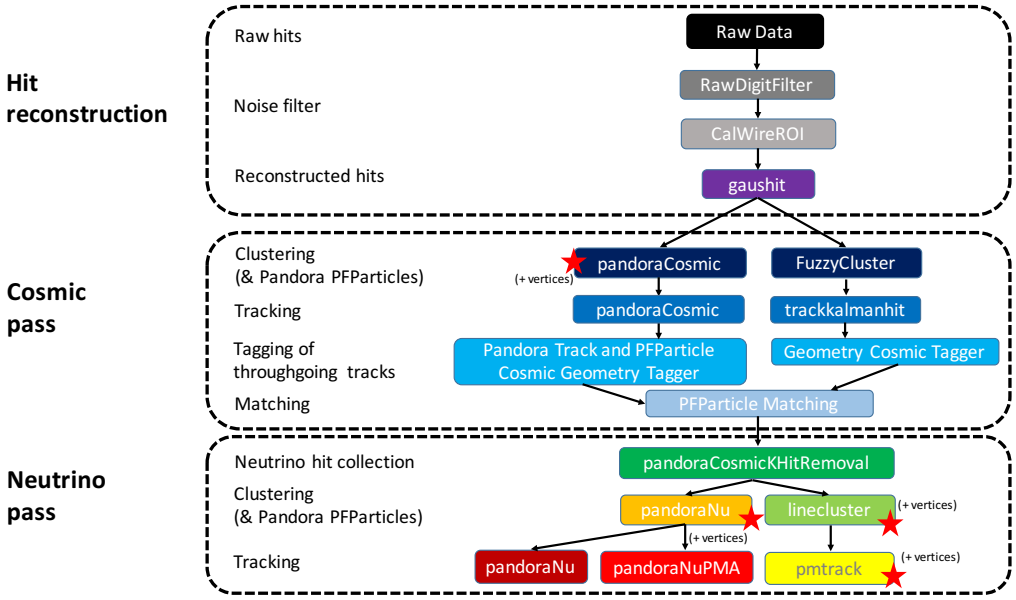

Figure 2: Reconstruction chain for data and MC processing. The red stars on some of the boxes indicate that the algorithms return reconstructed 3D vertices.

3.2.2 Treatment of noise and unresponsive wires in simulation and impact on data/MC agreement

A variety of different sources and forms of noise on the TPC wires has been observed in the MicroBooNE data [5]. The noise model used in the simulation in this note does not yet reflect all different sources observed in data. It is a simple white noise model, that in particular doesn't account for correlated noise. This is a clear deficiency of current MC simulation and studies are ongoing to improve noise modeling in the near future.

Software noise filtering is applied to both, data and simulation, in the same way. The noise filtering has selection cuts on particular forms of noise, which – if these are not present in the simulation because they were not simulated – are not always effective on the simulation. At present, there is no quantitative study on how noise affects the reconstruction of high level variables such as tracking and vertexing. Different noise effects are being subsequently added to the detector simulation and their impact on the reconstruction will be carefully studied. The largest contributors to the calorimetry calibration factors are expected to be the field response function used in deconvolution, the electron lifetime calibration, and the performance of the hit finder. The role of the noise on this should be limited (other than the touching wires, which again modify the local E-field, thus modifying the field response functions). We developed a new procedure of signal processing, and we are in the process of improving this in the upcoming baseline simulation not yet used in this note [6]. Another uncertainty on the calorimetric reconstruction is coming from the recombination of drift electrons. Calibration studies for this effect are currently ongoing.

The calibration variables are used in selection II for cosmic removal, but they are not used anywhere for calorimetric measurements. Selection II has been tested for robustness towards varying overall scaling of calorimetry calibration constants in the range of 10% to 30%, and has shown that the impact is rather small: The change on the number of selected events is of the order of 1%.

The detector also has a set of wires which are considered unresponsice, because the wires are either very noisy, the channels on the ASICs are unresponsive or the wires don't seem to be connected to the ASICs, or quiet, because they show only weak signals. The total number of wires considered unresponsive is 862 [5], which corresponds to about 10% of the

total number of wires in the detector. The majority of these are permanently unresponsive. About 10% show intermittent behavior, which means varying amounts of noise observed over time. The number of quiet wires is a lot smaller. It is around 1-2% of the total number of wires, but fluctuates over time.

The simulation uses a static list channel of unresponsive channels, and channels on this list are treated as non-existing during the reconstruction. This is done in both, reconstruction of data as well as simulation.

It has been observed that unresponsive wires in the detector lead to so called broken tracks, which arises from clusters not being merged across gaps of unresponsive wires. This results in tracks being reconstructed occasionally with shorter length since part of them are list in a region of unresponsive wires. However, only two functioning wire planes are required for event reconstruction, the third wire plane is adding redundant information if it is functioning. Both reconstruction algorithms used here, PMA and pandora, only require clusters in two planes in order to create three-dimensional reconstruction objects such as tracks and vertices, and therefore are less impacted by unresponsive wires. The pandora algorithms have been modified to include the information if the third plane has an unresponsive or functioning region in the questionable range when assembling tracks from two-dimensional cluster objects of two planes.

3.2.3 Reconstruction performance

The reconstruction results used in both event selections presented in this note are tested for agreement between data and simulation [18]. This includes the flashes, tracks and vertices. Despite the deficiencies of the current simulation as mentioned in Section 3.2.2, the agreement between data from the off-beam stream and cosmic background simulation has been shown to be reasonably good. Spatial distributions such as the distributions of start and end points of tracks and vertices in the detector appear well modeled in the simulation and even regions with a known high density of unresponsive wires cause equally pronounced features in data and simulation. Most difficulties are observed in the modeling of calorimetric distributions with differences of the order of 10% to 30% between data and simulation in the absolute calibration. However, as mentioned before, the selection II presented here has been shown to be robust against these offsets. Studies to improve the calorimetric calibrations using Michel electrons [19], crossing muons and $\pi^0 \to \gamma\gamma$ events are currently ongoing.

The track reconstruction performance based on an evaluation of simulation is shown in Figure 3a. The tracking efficiency for muons from neutrino interactions with vertex inside the fiducial volume is defined as

$$\epsilon = \frac{\text{Events with } \nu\text{-induced muon reconstructed track}}{\text{Generated events with true } \nu\text{-induced muon track}}. \quad (1)$$

All reconstructed neutrino-induced muon tracks count using this efficiency definition, independent of whether the track was correctly reconstructed over its entire length or potentially broken up. To understand the impact of this requirement, Figure 3b shows the track length resolution for reconstructed neutrino-induced muon tracks. Figure 3a shows that for reasonably long muon tracks, the reconstruction performs well. Shorter tracks are more challenging and efforts are on-going to improve track reconstruction. Broken tracks are what causes the tail of the length resolution curve in Figure 3b. The simulation used for this study is overlaid with simulated cosmic background events.

4 Event selections

4.1 Selection schemes

As mentioned before, two event selections were developed in parallel, both relying on different strategies and reconstruction algorithms. Comparisons between both allowed cross-checks of

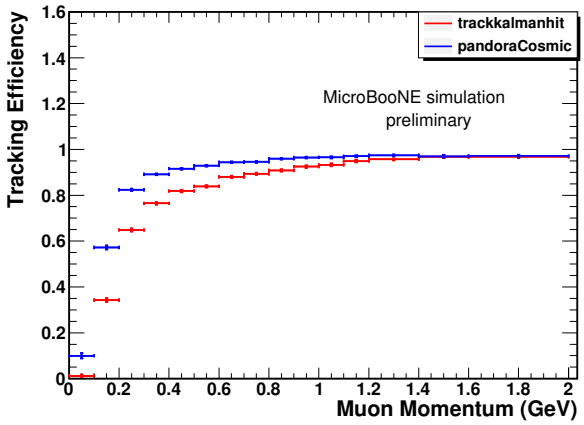

(a) Tracking efficiency for muons.

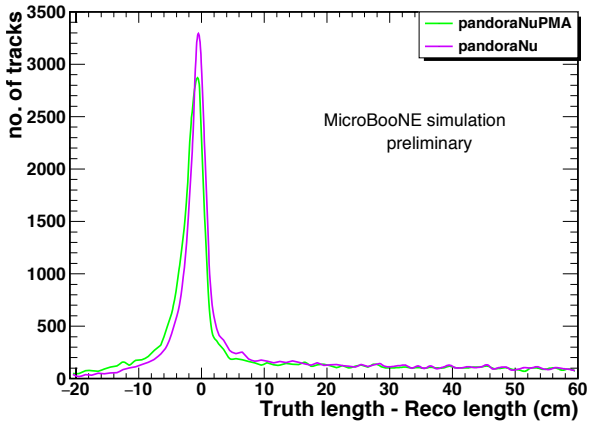

(b) Muon track length resolution

Figure 3: Tracking performance plots for muons for reconstruction algorithms used in the analysis. Figure 3a shows the tracking efficiency as defined in Equation 1 as a function of the momentum. Both algorithms (pandoraCosmic and trackkalmanhit) are used in order to remove through-going cosmic-ray muon tracks. Figure 3b shows the track length resolution for muons for the algorithms pandoraNu and pandoraNuPMA, which are used in the neutrino event selection and in the display of muon kinematic distributions of the selected events in Section 4. More detailed tracking efficiency studies for the Pandora algorithms can be found in [7].

the results and features observed in data and MC comparisons. Selection I is largely based on cuts developed in a MC performance study for a ν_μ CC inclusive cross section measurement [8]. It aims at identifying the muon from a neutrino interaction and doesn't bias towards track multiplicity. The reconstruction of the relatively long muon tracks is currently also at a more advanced stage and comparisons between data and simulation have shown good agreement for basic tracking variables such as the spatial distribution of tracks in the detector and track lengths [18]. However, in order to sufficiently reduce the cosmic background, the analysis is strongly biased towards forward-going tracks and requires containment in the TPC fiducial volume. This limits the phase space and reduces the acceptance. Selection II chooses a different and more complex approach. Different strategies are applied for single track events and events with higher track multiplicity. While the selection for single tracks follows similar ideas as selection I, it makes additional use of calorimetric track information which reveals information on the track direction. Given the problems mentioned in Section 3.2.2, however, the calorimetry is currently still more challenging for both simulation and reconstruction. For track multiplicities ≥ 2, cosmic background suppression is easier and the selection opens up for exiting events, which significantly improves the acceptance.

The selection schemes are illustrated in Figure 4. Both selections start with the same cut, requiring an optical flash (see Section 3.1) during the previously calibrated beam window with a duration of 1.6 μs. This is illustrated in Figure 5. Both selections make use of the optical information again later on, which is the so called flash-track-matching: candidate neutrino-induced tracks are tested for their distance from the observed flash using the PE-weighted center of the flash in the Z-direction. Due to the spatial distribution of PMTs on the detector anode side the resolution in Z is a lot better than the resolution in Y.

Only tracks starting within a certain distance of a reconstructed vertex are further considered as neutrino candidates. Vertices, however, are often also reconstructed at the start points of cosmic tracks or knots of decays or interactions. Reconstructed vertices are required to be contained in the fiducial volume of the detector, which is defined as 10 cm from the border of the active volume in X (20 cm for selection II), 10 cm from the border of the

active volume in Z, and 20 cm from the border of the active volume in Y. The same fiducial volume definitions are used when track containment is required.

In order to further reduce cosmic background in particular for single track events, selection I is choosing the most forward-going interaction, by determining a momentum-like quantity given by averaging the direction of all tracks originating from this vertex weighted with their track length. This cut decreases the phase space in $\cos(\theta)$ as can be seen from Figure 8. Both selections show a distortion of the acceptance in ϕ, which is introduced by the tagging and removal of through-going tracks in the reconstruction chain (see Figure 2). The ϕ-distribution of neutrino induced muon candidates would otherwise be flat. Selection II has an additional cut on vertical tracks to further reduce cosmic background for single tracks through a cut on track direction or the length of the vertical projection of the track. This causes the distortion of the acceptance in ϕ to be even larger (see Figure 11).

The track length for contained events is an estimator of the track momentum. Therefore, the track length cuts in both selections directly translate into a momentum threshold that can be observed in Figure 6 and 7. Note that both selections use slightly different definitions for the track length: selection I displays and cuts on the track range, which is the three-dimensional distance between the track end points, while selection II uses the actual length along the reconstructed track trajectory points. In the future, one can make use of this relation for contained events for presenting distributions and cross section measurements as a function of the muon momentum. For exiting events, the muon momentum measurement has to rely on other estimates, which are currently being developed.

Selection II further distinguishes between tracks with track multiplicity = 2 and track multiplicity > 2. All events with track multiplicity > 2 pass the selection since cosmic backgrounds are sufficiently small in this subset. The largest background observed for events with multiplicity = 2 arises from muon decays into Michel electrons and tracks that get broken by the reconstruction (see Section 3.2.2). Broken track segments are typically almost parallel to each other and pointing into the same direction. They can be removed by a cut on the opening angle of $\cos(\alpha) < 0.95$. Muon decay backgrounds are removed in three steps:

1. It is checked whether the vertex is at the start or end of the longer (likely muon) track based on the observed energy loss distribution along the track. The start of the longer track is defined as the end with smaller energy loss dE/dx, the end is defined as the track end with larger energy loss. If the vertex is found at the end with the larger energy loss dE/dx, this is a hint that longer track could be a cosmic muon and the vertex marks the decay into a Michel electron.

2. If the track is vertical with the vertex inside the FV but the end of the longer track outside of the FV in Y this is a hint that the longer track could be an entering cosmic muon

3. If either condition (1) or condition (2) are fulfilled, and the track length of the shorter track is found to be smaller than 30 cm, the event is tagged as a muon decay with a Michel electron and removed from the selection.

Selection II at this point allows multiple neutrino interaction candidates per event to pass, which affects about 3% of the events. For these, a selection is made to choose the neutrino interaction candidate with the longest associated candidate muon track. As the very last step of the selection, an additional minimum track length requirement of 15 cm is placed on the candidate muon track in all events.

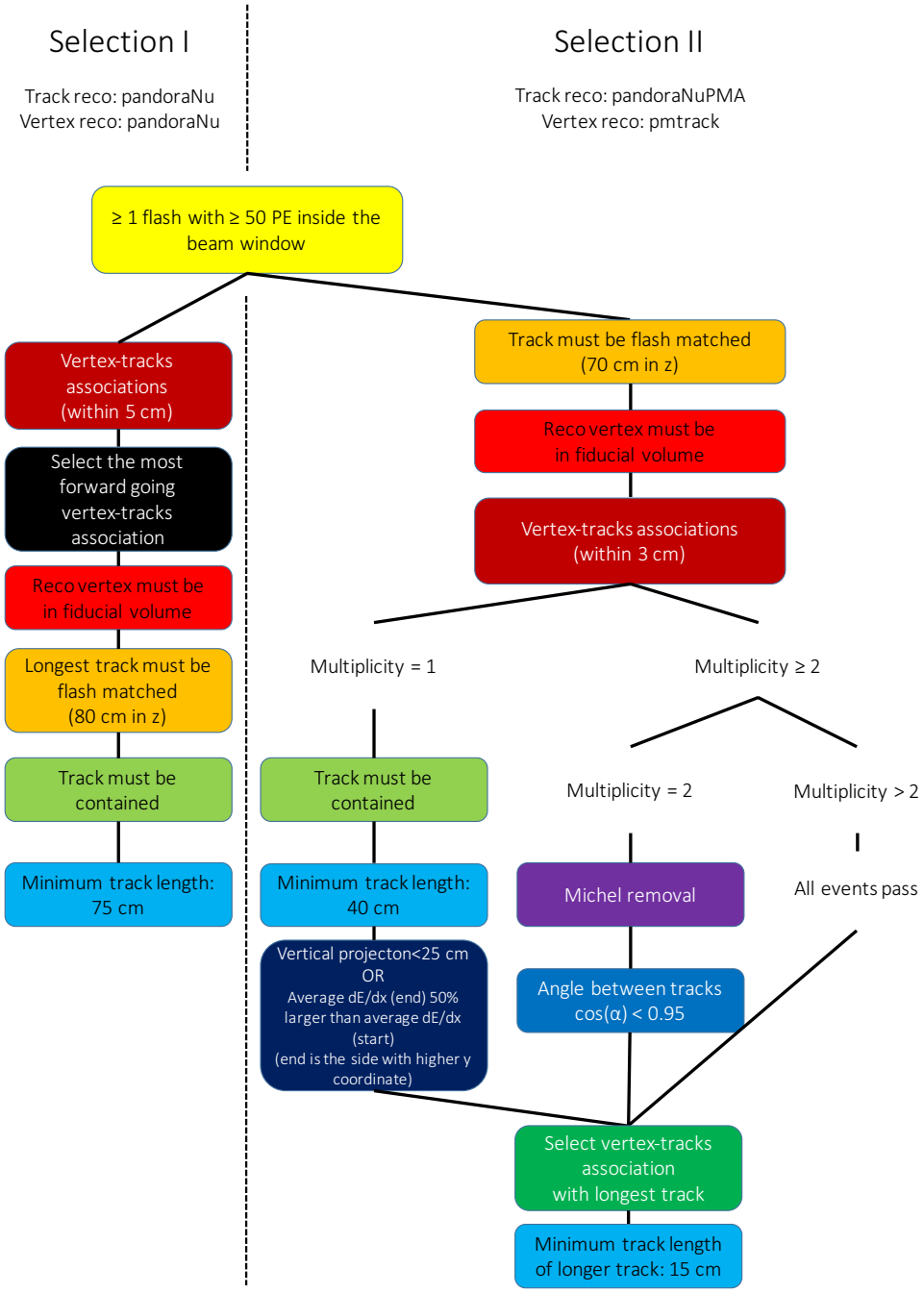

Figure 4: Event selection diagram for selections I and II, illustrating the different paths. Both selections start with the exact same cut requiring a flash in the beam window using the same flash reconstruction. Boxes in the same color symbolize similar cuts (not necessarily the same cut values) for different paths.

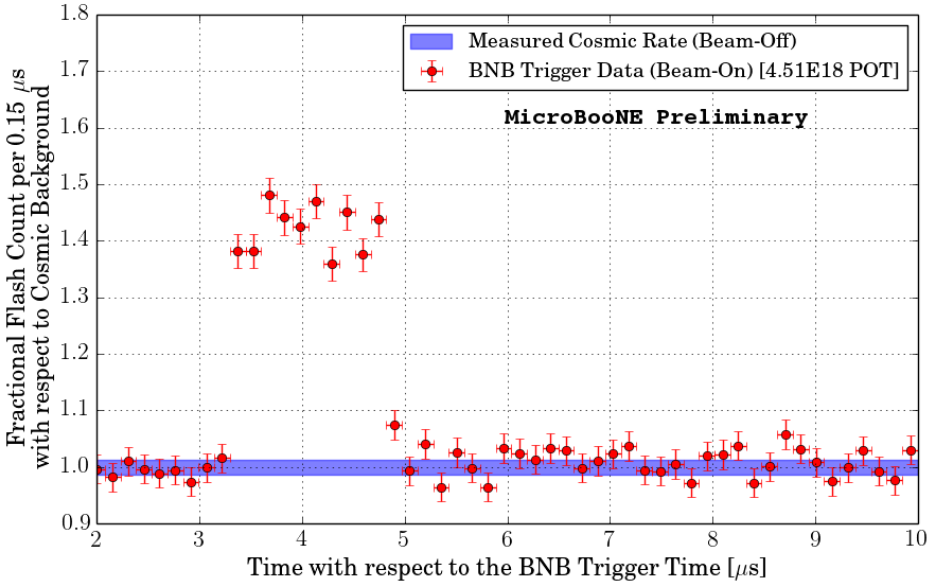

Figure 5: Time-distribution of reconstructed optical flashes with a PE value of 50 or more (no optical trigger applied). A clear excess in coincidence with the BNB spill is observed. The passing rate for a 50 PE threshold for the on-beam stream is around 25% (see Tables 1 and 2). The details of this analysis can be found in [4].

Table 1: **Selection I**: The table shows passing rates for the previously described event selection applied to on-beam and off-beam data. The numbers in brackets give the passing rate w.r.t. the step before (first percentage) and w.r.t. the generated events (second percentage). Note that the off-beam data stream has been scaled with a factor 1.23 to normalize to the on-beam data stream.

	on-beam		off-beam		
			measured	[scaled]	
Triggered	546910		388471	[477819]	
≥ 1 flash with ≥ 50 PE	135923	(25%/25%)	78657	[96748]	(20%/20%)
≥ 1 track within 5 cm of vertex	134744	(99%/25%)	77868	[95778]	(99%/20%)
vertex candidate in FV	74827	(55%/14%)	41844	[51468]	(54%/11%)
flash matching of longest track	22059	(29%/4.0%)	9946	[12234]	(24%/2.6%)
track containment	10722	(49%/1.9%)	4295	[5283]	(43%/1.1%)
track ≥ 75 cm	3213	(30%/0.6%)	1080	[1328]	(25%/0.3%)

4.2 Passing rates, efficiencies and phase space coverage

Efficiencies and purities of the selections are determined entirely from simulations, using generated BNB neutrino interactions overlaid with simulated cosmic background.

The efficiencies are about 12% for selection I and about 30% for selection II. These efficiency factors merge the acceptance and the selection efficiency. Therefore, the containment requirement for selection I is a large contribution to the low efficiency quoted for selection I. About a third of neutrino interactions in MicroBooNE are expected to generate a fully contained muon track.

Purities are about 55% for selection I, and 65% for selection II. The purity estimation counts all true ν_μ CC interactions with a vertex inside the fiducial volume that are correctly identified by the selection as signal, and any other beam-related and cosmic backgrounds as background. Data driven studies are on-going to improve and verify these simulation based estimates.

The selected signal events from a BNB + Cosmic simulation from both selections were compared in order to study the overlap between the two samples. For this comparison, only fully contained muon candidate tracks from selection II were considered, events from selection I do all have a fully contained muon candidate track by definition. The overlap of correctly selected ν_μ CC signal events between both samples is one third, which shows that the different strategies are sensitive to different topologies. It was also found that selection II selected about 15% more events with a fully contained muon candidate track than selection I.

Passing rates for on- and off-beam data for selections I and II can be found in Tables 1 and 2. The on-beam data stream contains all signal, beam-related and cosmic backgrounds. The off-beam data stream is used for subtraction of pure cosmic backgrounds. Subtracting off-beam from on-beam data results in an excess of 1885 ± 70 events for selection I and 2700 ± 62 events for selection II. This shows clearly that the automated selection is selecting beam-related events in a large numbers. As mentioned previously, the excess in selection II is larger since selection II has a higher purity and less pure cosmic background.

Figures 6 to 11 show muon kinematic truth distributions for the ν_μ CC signal broken up into various physics processes (using GENIE process definitions). The intrinsic BNB ν_μ CC spectrum comprises of $\sim$ 60% quasi-elastic (QE), $\sim$ 30% resonant (RES) and $\sim$ 10% deep inelastic (DIS) interactions. The final selections constitute of 51% QE, 37% RES, and 11% DIS for selection I, and 43% QE, 42% RES, and 14% DIS for selection II. The larger contribution of RES and DIS events in selection II arises from the inclusion of exiting tracks. These tracks typically have higher momentum and hence indicate a higher initial neutrino energy.

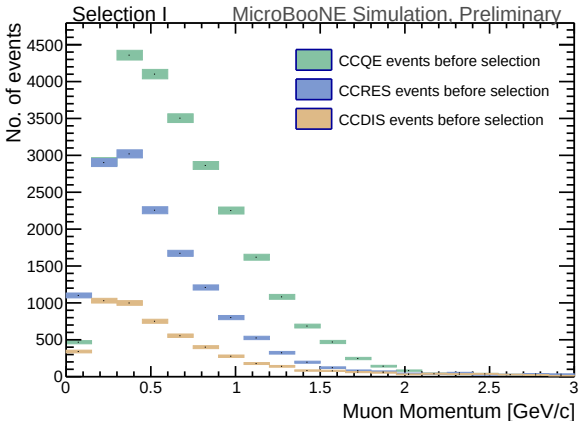

(a) Selection I: Momentum distribution before selection.

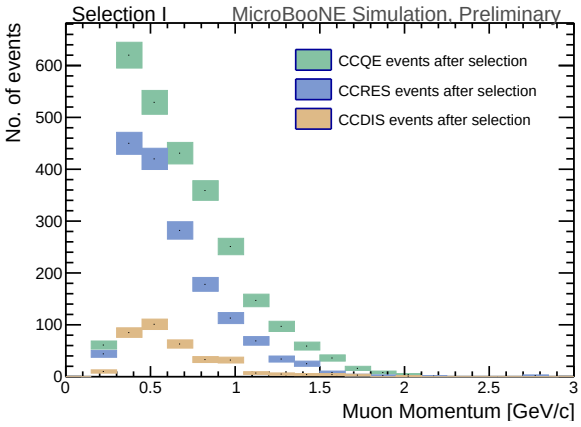

(b) Selection I: Momentum distribution after selection.

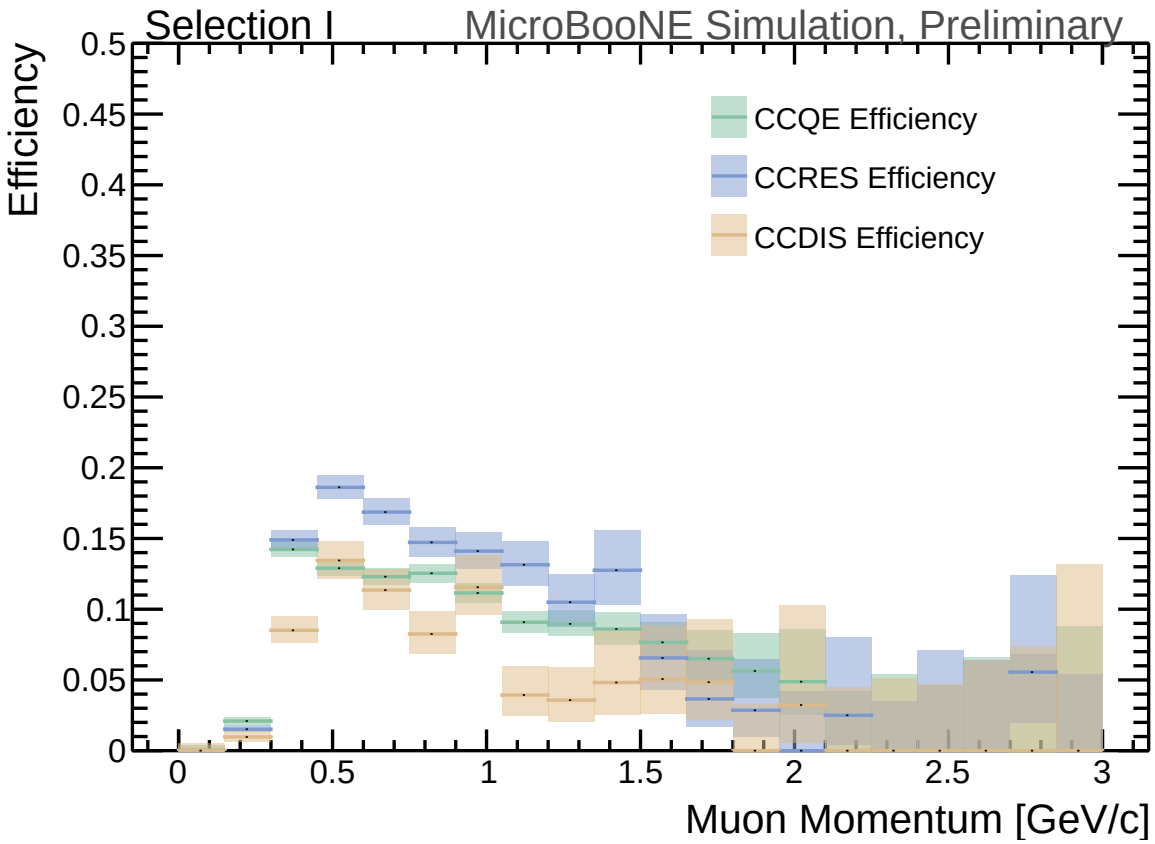

(c) Selection I: Selection efficiency as a function of the true muon momentum.

Figure 6: Top: lepton track momentum (truth) distribution before (6a) and after (6b) the selection for selection I. Bottom: the efficiency of the selected events for the processes quasi-elastic (QE), resonant (RES), and deep-inelastic (DIS). The bands represent the statistical uncertainty only. The distributions are shown as a function of the true muon momentum. The rise of the efficiency between 0 and 0.5 GeV is caused by the minimum track length cut, which directly translates into a cut on the muon momentum. The decreasing efficiency for higher momentum tracks is caused by the containment requirement.

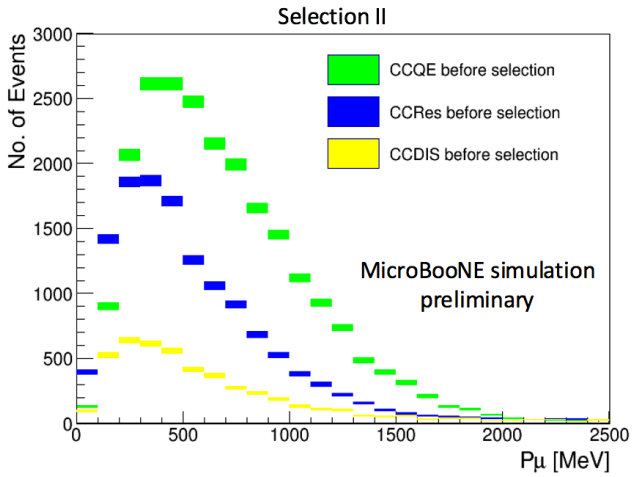

(a) Selection II: Momentum distribution before selection.

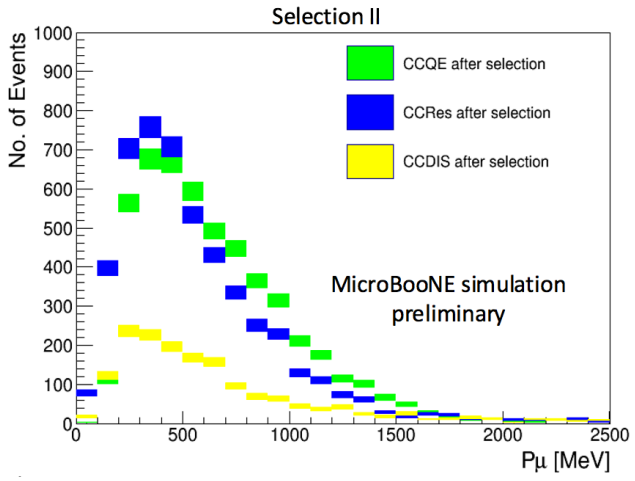

(b) Selection II: Momentum distribution after selection.

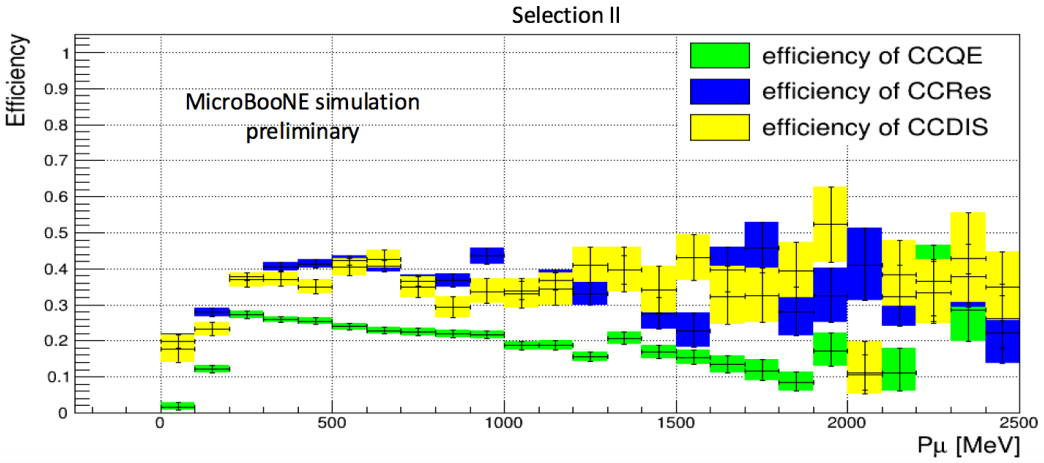

(c) Selection II: Selection efficiency as a function of the true muon momentum.

Figure 7: Top: lepton track momentum (truth) distribution before (7a) and after (7b) the selection for selection II. Bottom: the efficiency of the selected events for the processes quasi-elastic (QE), resonant (RES), and deep-inelastic (DIS). The bands represent the statistical uncertainty only. The distributions are shown as a function of the true muon momentum. The rise of the efficiency between 0 and 0.5 GeV is caused by the minimum track length cut, which directly translates into a cut on the muon momentum. There is no decrease in the efficiency for higher momentum RES and DIS events, because there is no containment requirement for events with a track multiplicity ≥ 2.

Table 2: **Selection II**: The table shows passing rates for the previously described event selection applied to on-beam and off-beam data. The numbers in brackets give the passing rate w.r.t. the step before (first percentage) and w.r.t. the generated events (second percentage). Note that the off-beam data stream has been scaled with a factor 1.23 to normalize to the on-beam data stream. Please note that after flash track matching, the sample is split into different branches with individual cuts, and combined at final stage (see Figure 4).

	on-beam		off-beam		
			measured	[scaled]	
Triggered	546910		388471	[477819]	
≥ 1 flash with $\geq 50\,\mathrm{PE}$	135923	(25%/25%)	78657	[96748]	(20%/20%)
Flash track matching	86425	(64%/16%)	47754	[59737]	(61%/12%)
Track multiplicity>=2 after Michel removal	2191	(3%/0.4%)	267	[328]	(0.6%/0.07%)
Track multiplicity==1	1037	(1.2%/0.2%)	162	[199]	(0.3%/0.04%)
Final (combined track mult.)	3228	(3.7%/0.59%)	429	[528]	(0.9%/0.09%)

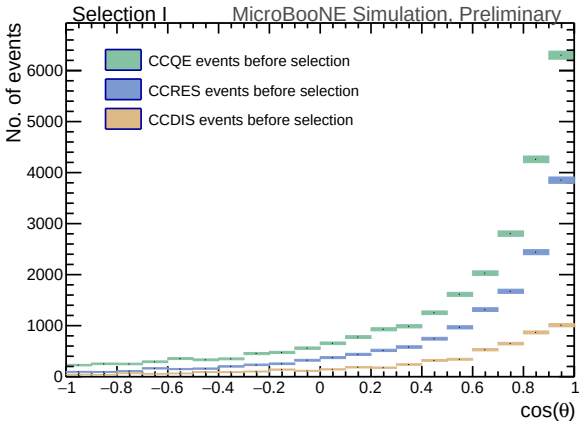

(a) Selection I: $\cos(\theta)$ distribution before selection.

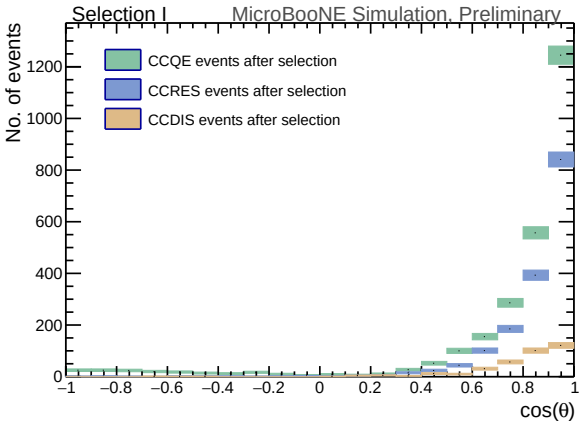

(b) Selection I: $\cos(\theta)$ distribution after selection.

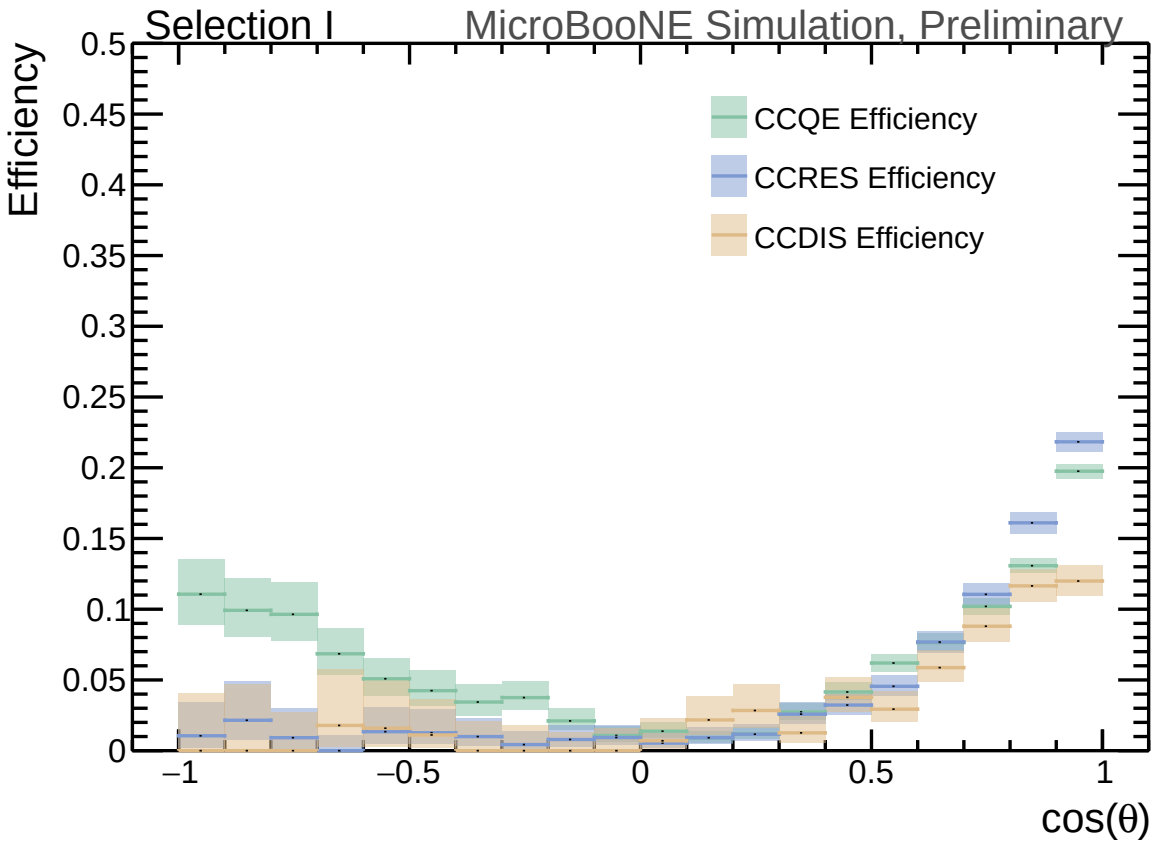

(c) Selection I: Selection efficiency as a function of the true muon angle $\cos(\theta)$.

Figure 8: Top: lepton track angle $\cos(\theta)$ (truth) distribution before (8a) and after (8b) the selection for selection I. Bottom: the efficiency of the selected events for the processes quasi-elastic (QE), resonant (RES), and deep-inelastic (DIS). The bands represent the statistical uncertainty only. Comparing figure 8a and 8b shows the decrease in phase space by the selection of mostly forward going events. This is also observed in the efficiency curve, which has a minimum for vertical tracks. Since the track direction is often flipped in the reconstruction, the efficiency is similar for forward and backward going muon tracks.

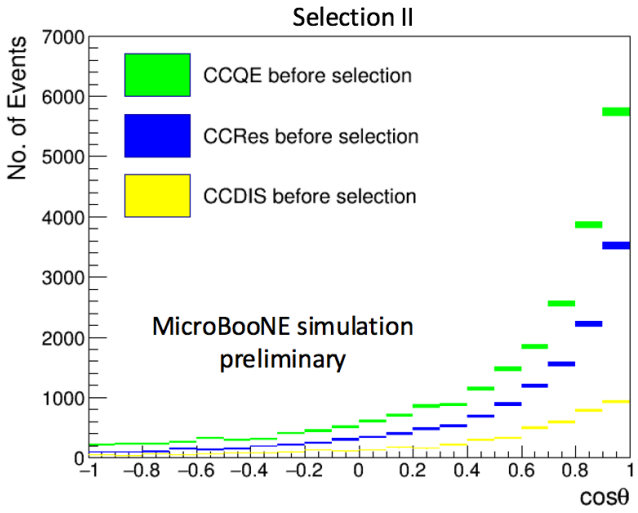

(a) Selection II: cos(θ) distribution before selection.

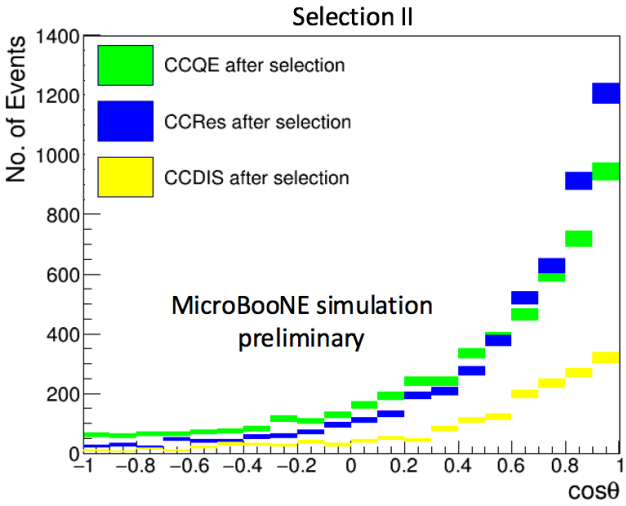

(b) Selection II: cos(θ) distribution after selection.

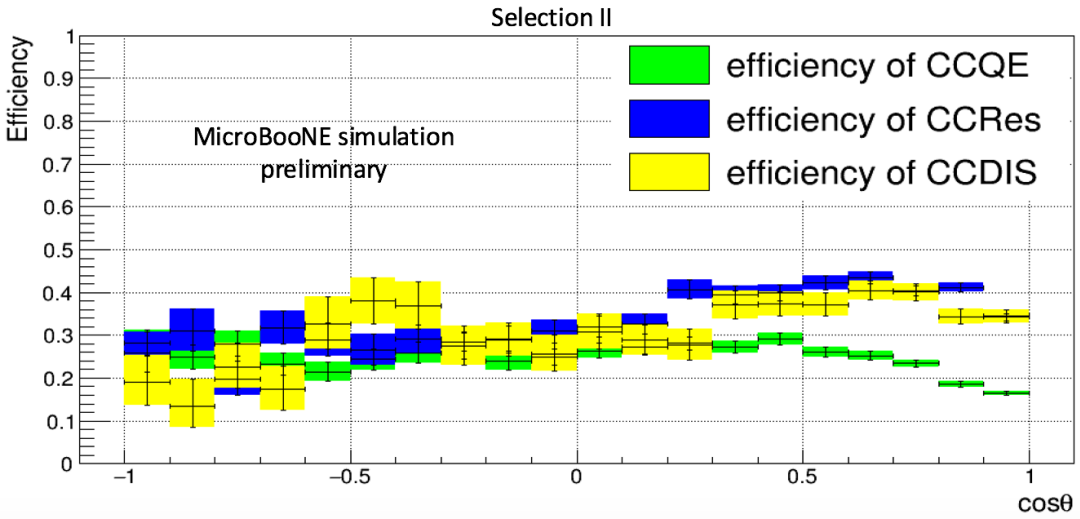

(c) Selection II: Selection efficiency as a function of the true muon angle cos(θ).

Figure 9: Top: lepton track angle cos(θ) (truth) distribution before (9a) and after (9b) the selection for selection II. Bottom: the efficiency of the selected events for the processes quasi-elastic (QE), resonant (RES), and deep-inelastic (DIS). The bands represent the statistical uncertainty only. The distributions are shown as a function of the true muon momentum. The phase space coverage for selection II is larger than for selection I (compare to Figure 8 and the efficiency is more flat in cos(θ)

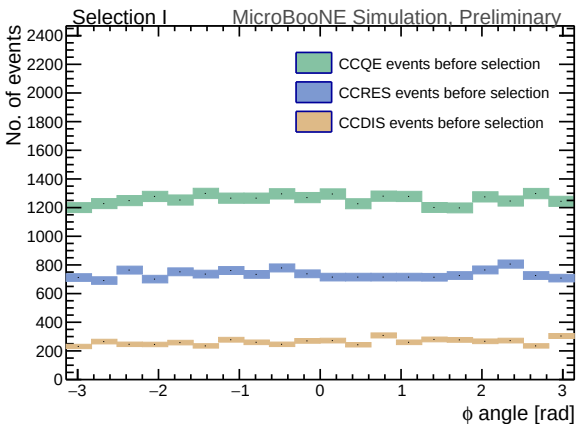

(a) Selection I: ϕ distribution before selection.

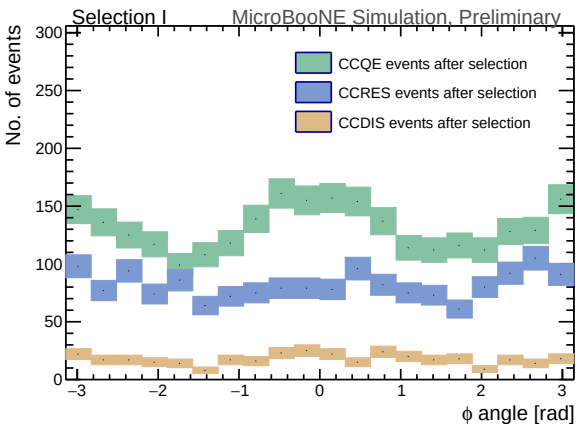

(b) Selection I: ϕ distribution after selection.

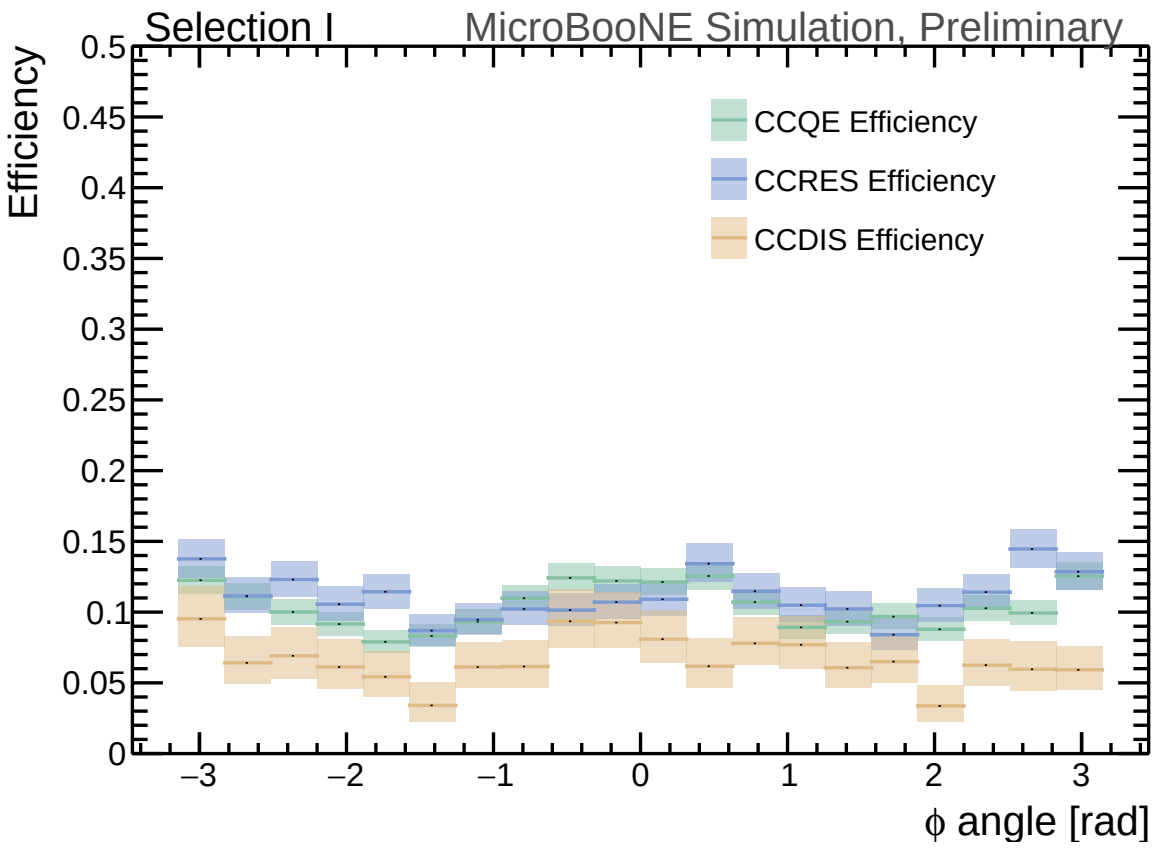

(c) Selection I: Selection efficiency as a function of the true muon angle ϕ.

Figure 10: Top: lepton track angle ϕ (truth) distribution before (10a) and after (10b) the selection for selection I. Bottom: the efficiency of the selected events for the processes quasi-elastic (QE), resonant (RES), and deep-inelastic (DIS). The bands represent the statistical uncertainty only. The containment requirements and cosmic removal cuts turn the originally flat distribution in ϕ into the characteristic shape observed in 10b.

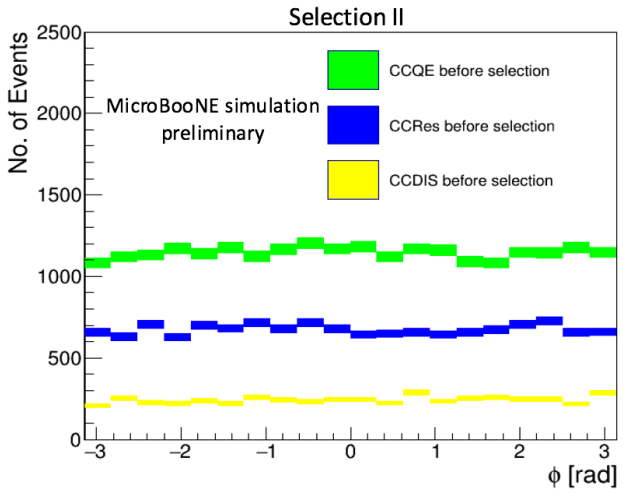

(a) Selection II: ϕ distribution before selection.

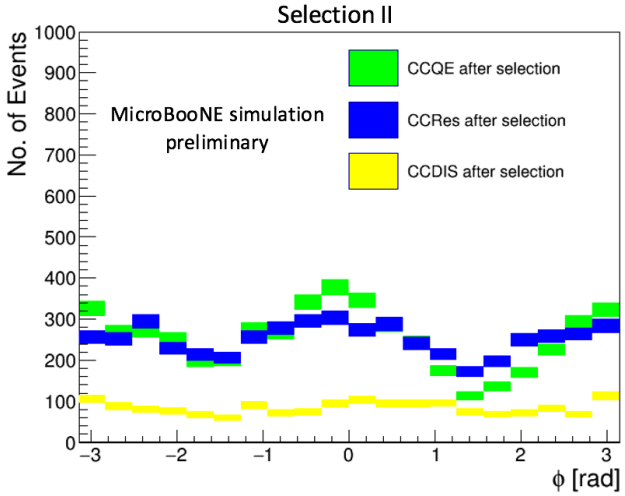

(b) Selection II: ϕ distribution after selection.

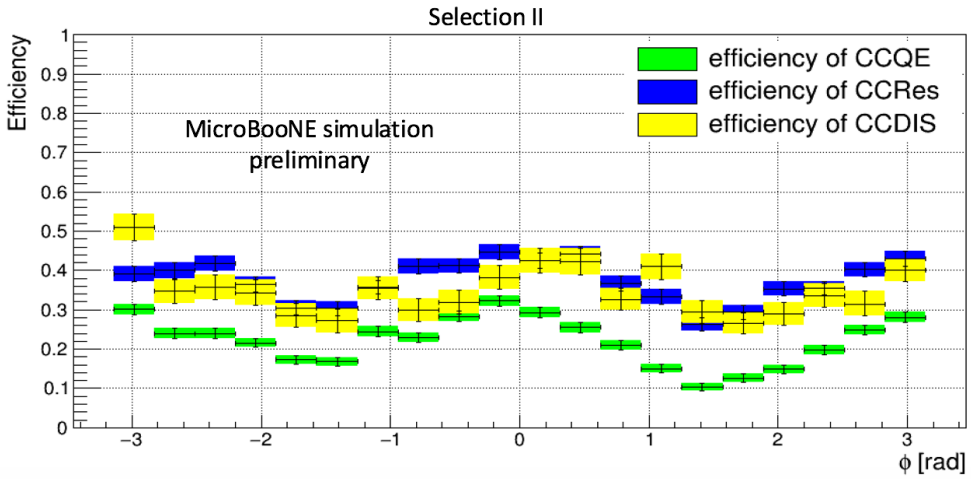

(c) Selection II: Selection efficiency as a function of the true muon angle ϕ.

Figure 11: Top: lepton track angle ϕ (truth) distribution before (11a) and after (11b) the selection for selection II. Bottom: the efficiency of the selected events for the processes quasi-elastic (QE), resonant (RES), and deep-inelastic (DIS). The bands represent the statistical uncertainty only. The distributions are shown as a function of the true muon momentum. The bands represent the statistical uncertainty only. The containment requirements and cosmic removal cuts turn the originally flat distribution in ϕ into the characteristic shape observed in 11b.

4.3 Kinematic distributions

Figures 12, 13, 14, and 15 show kinematic distributions of final events from selection I and selection II. The black data points show the difference between data taken when the beam was on and data taken when the beam was off from the good run sample defined in Section 2 with their statistical uncertainty. When subtracting data from the off-beam stream, the background of purely cosmic events is removed. Besides ν_μ CC signal events, the remaining data set still contains all beam related backgrounds (neutral current (NC) events, $\bar{\nu}_\mu$ interactions, or $\nu_e/\bar{\nu}_e$ interactions) as well as mis-identified events where a cosmic is mistaken for a neutrino interaction, which triggered the readout. These events are not removed by the off-beam subtraction. The data is compared to a simulation of BNB neutrino interactions overlaid with simulated cosmic background tracks, which includes the same types of backgrounds as the off-beam subtracted data. For now, the simulation is normalized to match the total selected event number in the data and therefore no conclusions on the overall normalization offset between data and simulation can be drawn at this point. The errors presented are statistical only.

The first thing to note when comparing the two selections is that the main background contribution to selection I are cosmics, while the main background contribution to selection II are NC events. The agreement between data and simulation in Figures 12 and 13 is good for both selections. As pointed out previously, selection II has a larger coverage in the θ-direction (the angle w.r.t. the beam direction, see Figure 1) which can be seen again in Figure 13. Figure 14 shows the ϕ distributions for both selections, which are expected to be flat for signal. It shows that if subtracting all backgrounds, both distributions wouldn't be flat in ϕ. This is a result of the removal of vertical cosmic tracks through selection cuts, which is more pronounced in selection II. Figure 14a shows a slight mismatch between the data and the simulation for angles of $\phi \sim -\pi$ and $\phi \sim \pi$. These are the angles of vertical tracks and indicate that some not well simulated cosmic background contribution is still present in the data. One way to address this problem is to generate neutrino event simulation samples overlaid with cosmic background tracks from actual off-beam data. This will prevent any mis-modeling of cosmic background in the simulation. The tools for such an overlay on MicroBooNE data are currently being developed.

Figures 15 shows the distribution of selected interaction vertices inside the detector projected on the X, Y, and Z-direction (for definitions of the coordinate system see Figure 1). For selection I, data and simulation agree within statistics. While the distributions in X and Y are relatively symmetric, the distribution in Z shows more vertices to be selected towards smaller values of z. This is the upstream end of the detector and the effect is explained by the majority of neutrino interactions following the beam direction. All distributions fall off towards the edges of the detector, which is caused by the containment requirement. The Y-distribution of selection II shows an asymmetry with more vertices selected with negative Y-values. This is the bottom half of the detector. The reason for this is that selection II makes use of track direction determined through the energy loss along the reconstructed track and downwards going tracks are more likely to be rejected. Therefore, more vertices are selected from the lower half of the detector. The Z-distribution of selection II has a very strong dip in both data and simulation at $\sim$ 750 cm. This is a region with a known high density of unresponsive wires in one of the planes (vertical wires) [5]. Less vertices are reconstructed within this region using the reconstruction algorithm PMA from selection II. Selection I doesn't show this feature, but is using a different reconstruction algorithm, pandoraNu. Comparisons of data and simulations in [18] have shown that pandoraNu is slightly less sensitive to this than PMA.

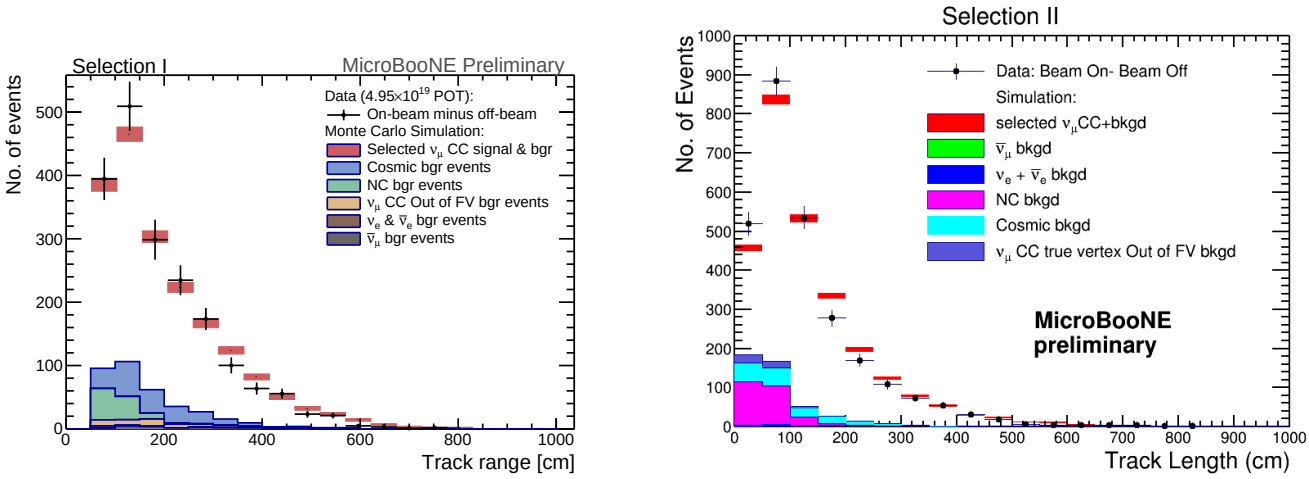

(a) Selection I

(b) Selection II

Figure 12: Track range/length distribution for both selections. The track range used in selection I is the three-dimensional distance between the track end points, the track length used in selection II is the actual length along the trajectory. In case of track multiplicities ≥ 2, the length of the longest track is shown. The black data points symbolize on-beam minus off-beam data with statistical error bars. The red shaded histogram represents the BNB+Cosmic MC, with the bands representing the statistical uncertainty on the MC. The backgrounds contained in the red are additionally shown in different colors corresponding to different physics processes. Backgrounds are stacked. Cosmic background represents the background of events that do contain a neutrino interactions but where a cosmic track is mis-identified as the neutrino induced muon candidate track. Purely cosmic background has been subtracted from the on-beam by subtracting off-beam data and therefore is not included in the simulation. The simulation is normalized to the same number of total events as the data.

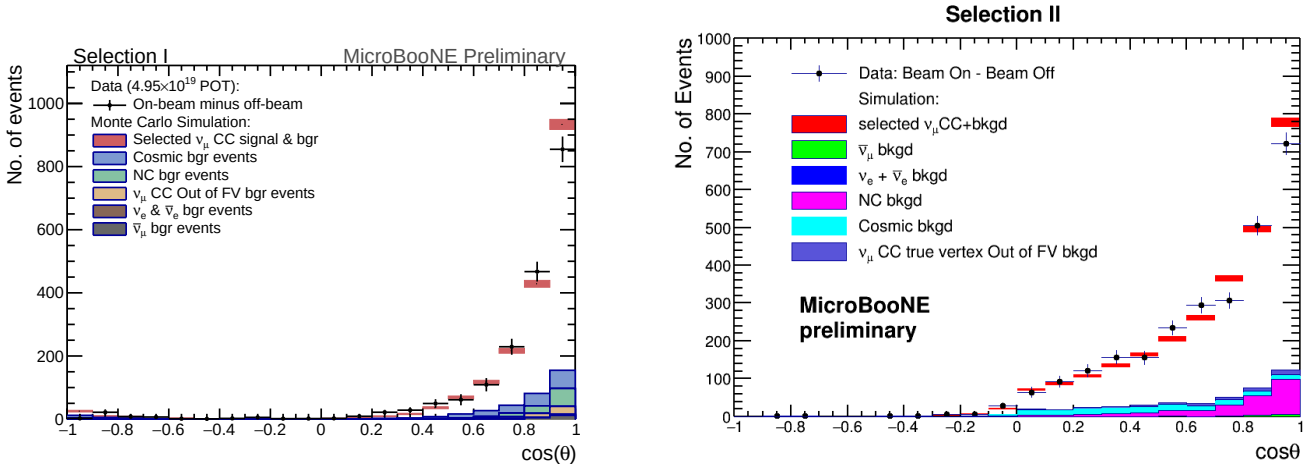

(a) Selection I (b) Selection II

Figure 13: Track $\cos(\theta)$ distribution for both selections. In case of track multiplicities ≥ 2, the angle of the longest track is shown. The black data points symbolize on-beam minus off-beam data with statistical error bars. The red shaded histogram represents the BNB+Cosmic MC, with the bands representing the statistical uncertainty on the MC. The backgrounds contained in the red are additionally shown in colors. Backgrounds are stacked. Cosmic background represents the background of events that do contain a neutrino interactions but where a cosmic track is mis-identified as the neutrino induced muon candidate track. Purely cosmic background has been subtracted from the on-beam by subtracting off-beam data and therefore is not included in the simulation. The simulation is normalized to the same number of total events as the data.

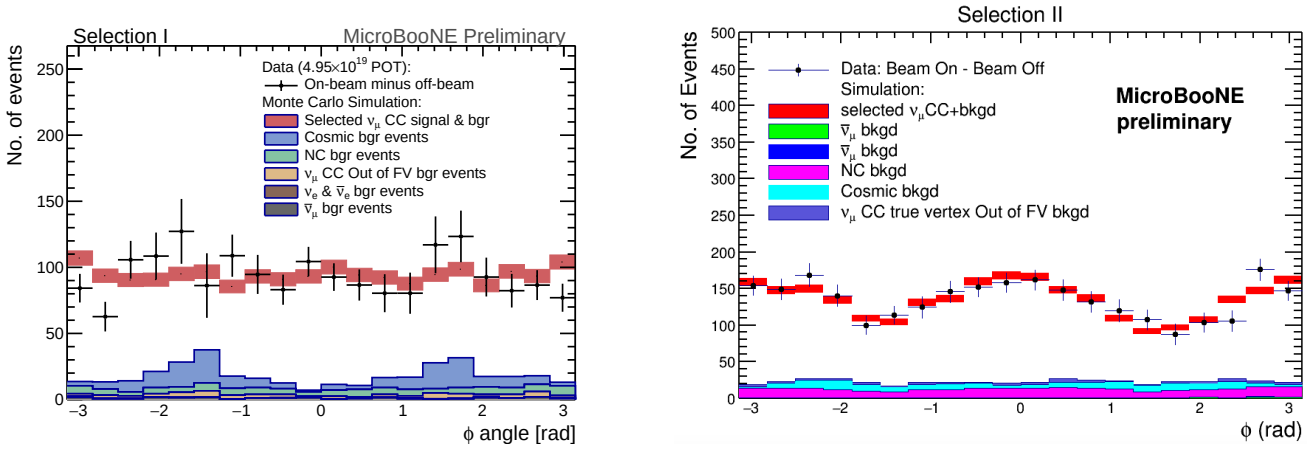

(a) Selection I (b) Selection II

Figure 14: Track ϕ distribution for both selections. In case of track multiplicities ≥ 2, the angle of the longest track is shown. The black data points symbolize on-beam minus off-beam data with statistical error bars. The red shaded histogram represents the BNB+Cosmic MC, with the bands representing the statistical uncertainty on the MC. The backgrounds contained in the red are additionally shown in colors. Backgrounds are stacked. Cosmic background represents the background of events that do contain a neutrino interactions but where a cosmic track is mis-identified as the neutrino induced muon candidate track. Purely cosmic background has been subtracted from the on-beam by subtracting off-beam data and therefore is not included in the simulation. The simulation is normalized to the same number of total events as the data.

5 Event Views

This section shows some event view from selected ν_μ CC candidate events from the on-beam stream. Figures 16 to 19 show events from selection I with various multiplicity, and Figures 20 to 23 show event views from selection II. The candidate interaction is shown in all three event views, and additional in a 3D event display showing the reconstructed tracks from pandoraNu (for selection I) and pandoraNuPMA (for selection II). These events were cherry-picked to include examples for various track multiplicities.

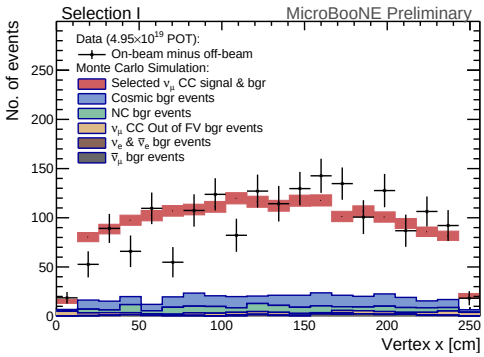

(a) Selection I: Vertex X

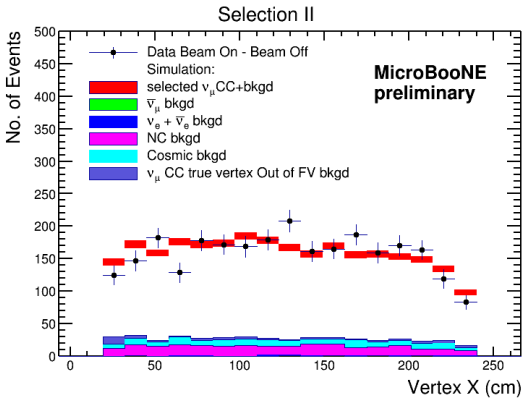

(b) Selection II: Vertex X

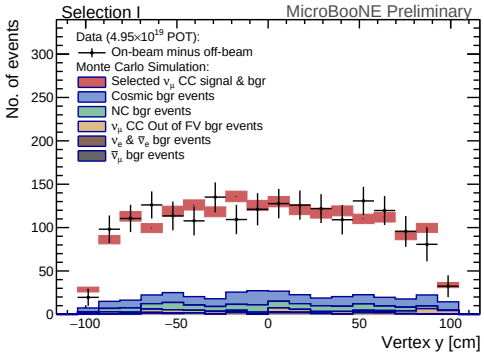

(c) Selection I: Vertex Y

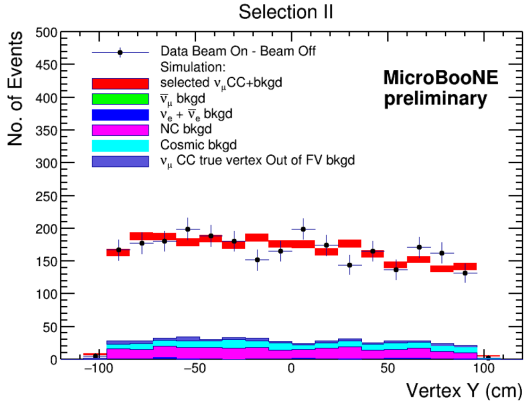

(d) Selection II: Vertex Y

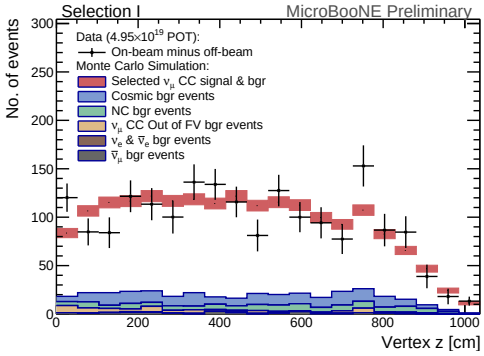

(e) Selection I: Vertex Z

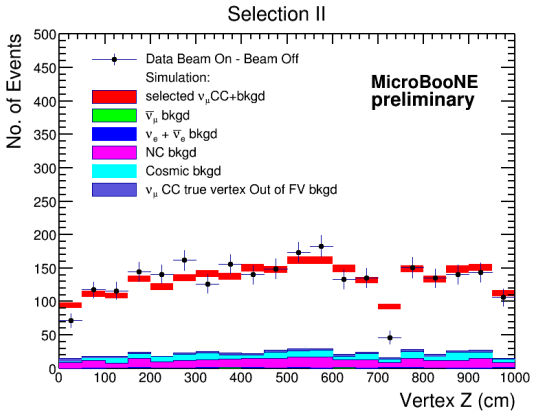

(f) Selection II: Vertex Z

Figure 15: Neutrino interaction candidate vertex distribution in the X, Y, and Z-coordinate for both selections. The black data points symbolize on-beam minus off-beam data with statistical error bars. The red shaded histogram represents the BNB+Cosmic MC, with the bands representing the statistical uncertainty on the simulation. The backgrounds contained in the red are additionally shown in colors. Backgrounds are stacked. Cosmic background represents the background of events that do contain a neutrino interactions but where a cosmic track is mis-identified as the neutrino induced muon candidate track. Purely cosmic background has been subtracted from the on-beam by subtracting off-beam data and therefore is not included in the simulation. The simulation is normalized to the same number of total events as the data.

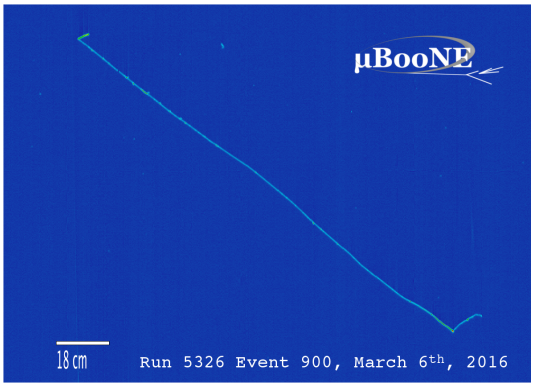

(a) Collection plane (Y)

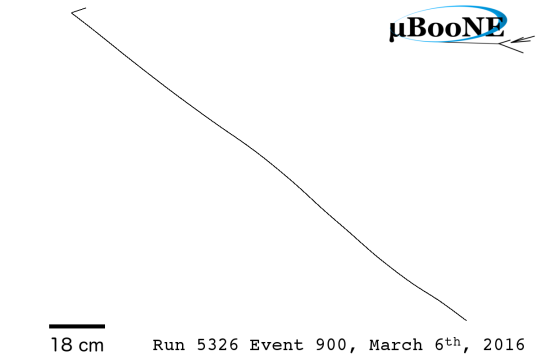

(b) Reconstructed 3D image (Y plane projection)

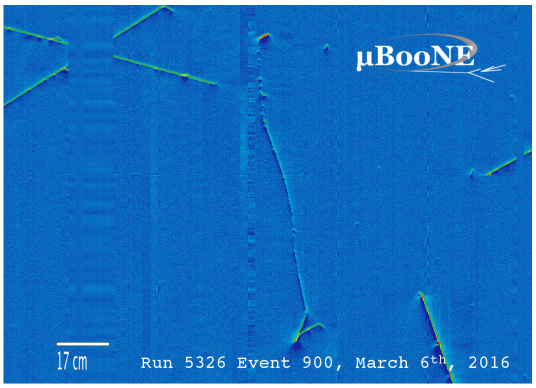

(c) Induction plane (U)

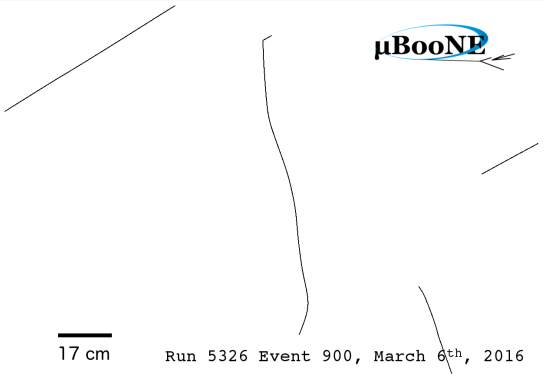

(d) Reconstructed 3D image (U plane projection)

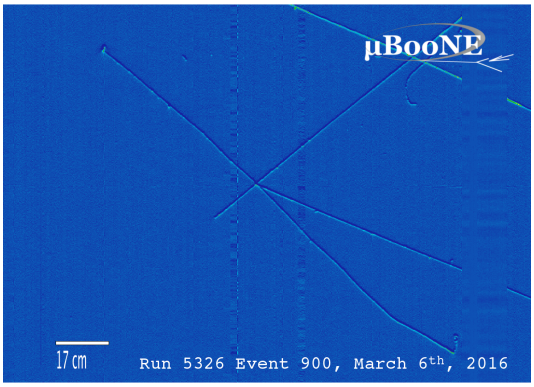

(e) Induction plane (V)

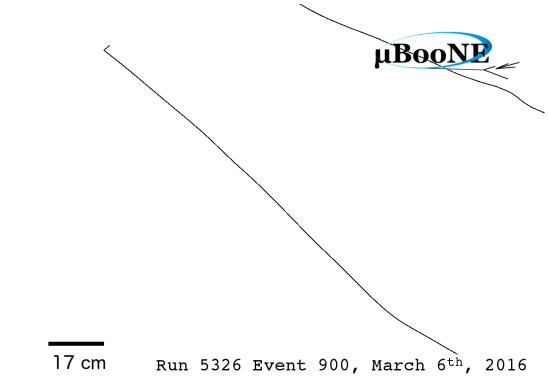

(f) Reconstructed 3D image (V plane projection)

Figure 16: Event view for run 5326, event 900, selected by selection I. The plots on the left show the event view in all three wire planes. The induction planes show features of gaps of unresponsive wires and noise (see e.g. left hand side of 16e). The plots on the right show the three-dimensional reconstructed image projected onto each wire plane. The track reconstruction algorithm shown is pandoraNu. All figures have the same scale (indicated by the bar in the bottom left) and aspect ratio.

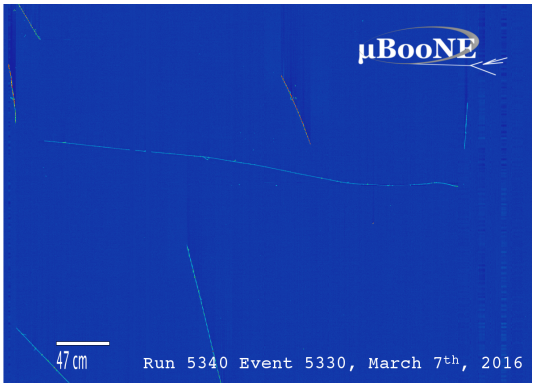

(a) Collection plane (Y)

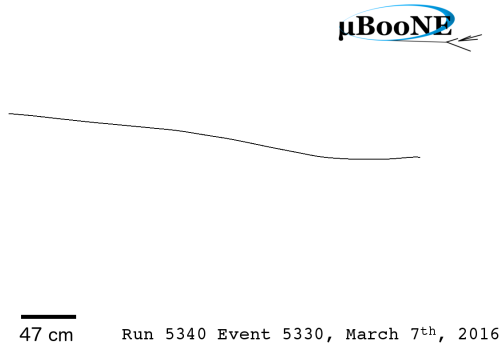

(b) Reconstructed 3D image (Y plane projection)

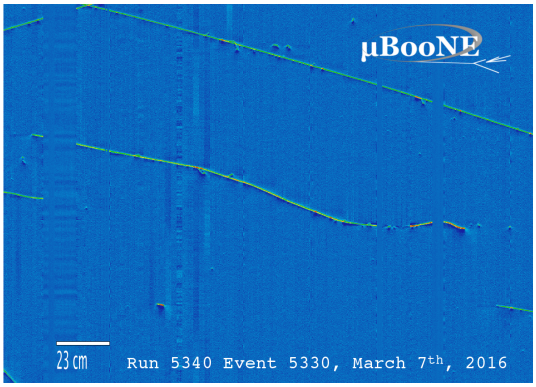

(c) Induction plane (U)

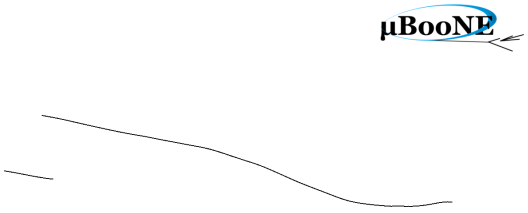

(d) Reconstructed 3D image (U plane projection)

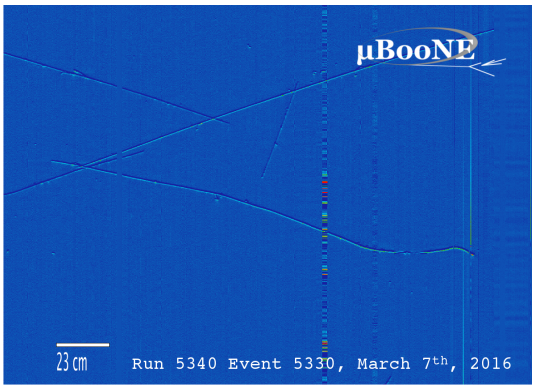

(e) Induction plane (V)

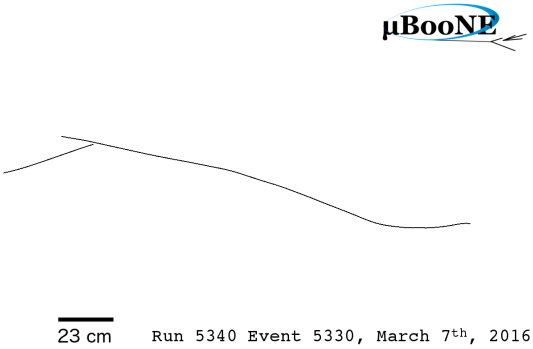

(f) Reconstructed 3D image (V plane projection)

Figure 17: Event view for run 5340, event 5330, selected by selection I. The plots on the left show the event view in all three wire planes. Both induction planes show noise (vertical stripes in Figures 17c and 17e. The plots on the right show the three-dimensional reconstructed image projected onto each wire plane. The track reconstruction algorithm shown is pandoraNu. Note that some tracks visible on the left hand plots are missing on the right because they have been rejected in the cosmic removal pass. All figures have the same scale (indicated by the bar in the bottom left) and aspect ratio.

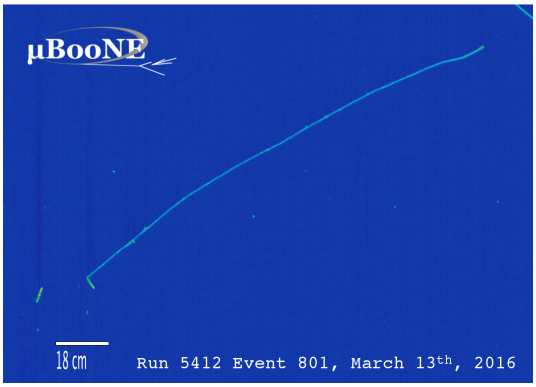

(a) Collection plane (Y)

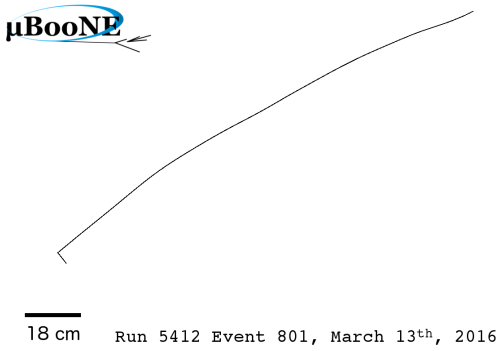

(b) Reconstructed 3D image (Y plane projection)

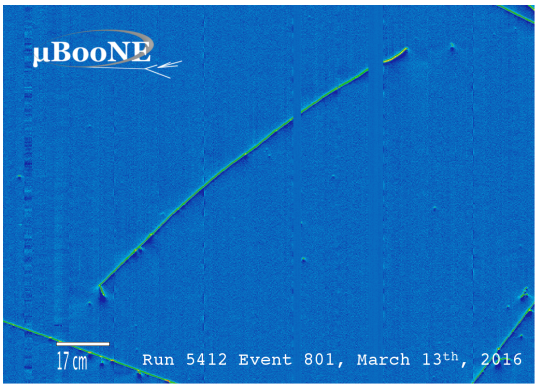

(c) Induction plane (U)

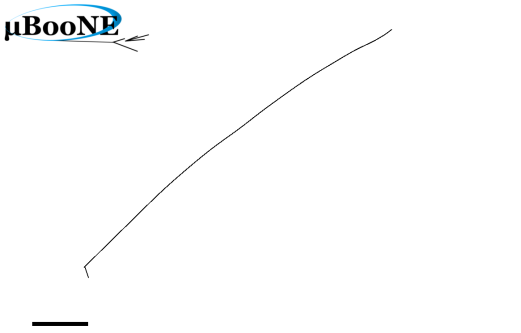

(d) Reconstructed 3D image (U plane projection)

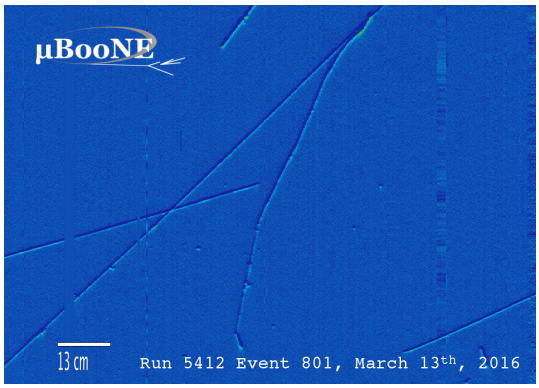

(e) Induction plane (V)

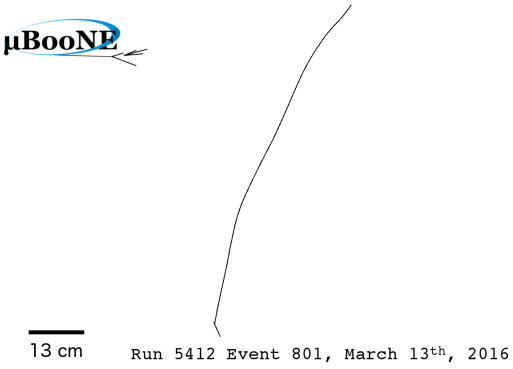

(f) Reconstructed 3D image (V plane projection)

Figure 18: Event view for run 5412, event 801, selected by selection I. The plots on the left show the event view in all three wire planes. The plots on the right show the three-dimensional reconstructed image projected onto each wire plane. The track reconstruction algorithm shown is pandoraNu. Note that some tracks visible on the left hand plots are missing on the right because they have been rejected in the cosmic removal pass. All figures have the same scale (indicated by the bar in the bottom left) and aspect ratio.

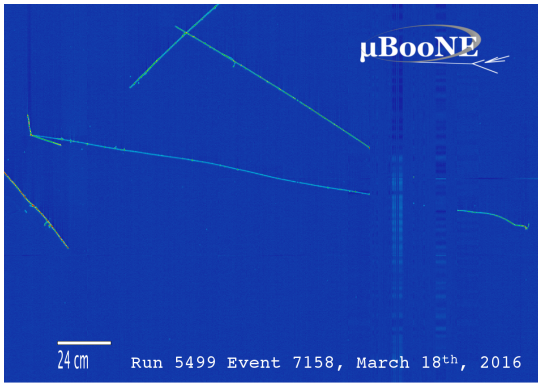

(a) Collection plane (Y)

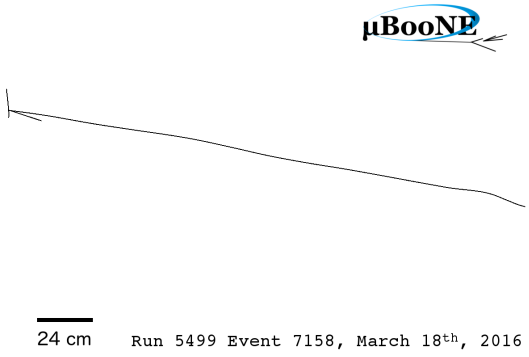

(b) Reconstructed 3D image (Y plane projection)

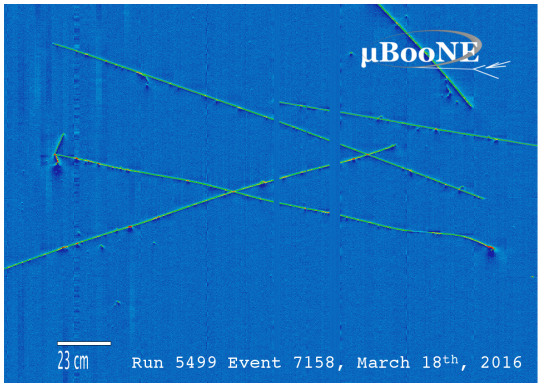

(c) Induction plane (U)

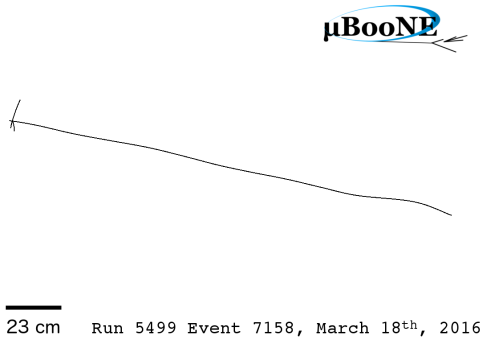

(d) Reconstructed 3D image (U plane projection)

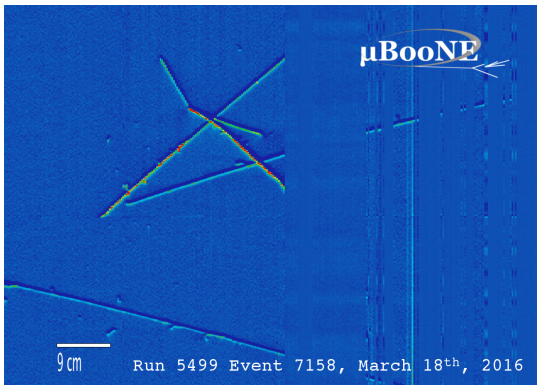

(e) Induction plane (V)

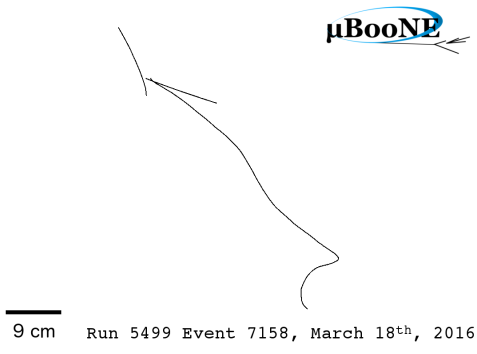

(f) Reconstructed 3D image (V plane projection)

Figure 19: Event view for run 5499, event 7158, selected by selection I. The plots on the left show the event view in all three wire planes. The Y and V plane show gaps of unresponsive wires and noise (see Figures 19a and 19e). The reconstruction successfully bridges these gaps. The plots on the right show the three-dimensional reconstructed image projected onto each wire plane. The track reconstruction algorithm shown is pandoraNu. Note that some tracks visible on the left hand plots are missing on the right because they have been rejected in the cosmic removal pass. All figures have the same scale (indicated by the white bar in the bottom left) and aspect ratio.

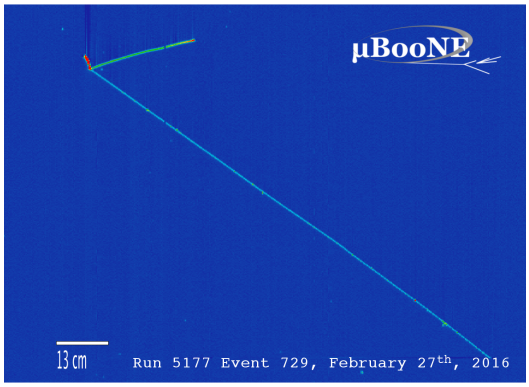

(a) Collection plane (Y)

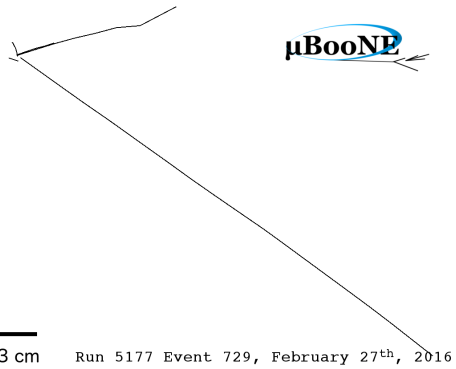

(b) Reconstructed 3D image (Y plane projection)

(c) Induction plane (U)

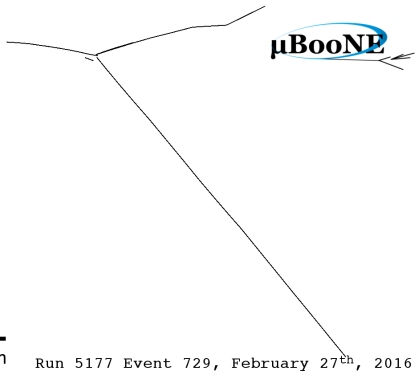

(d) Reconstructed 3D image (U plane projection)

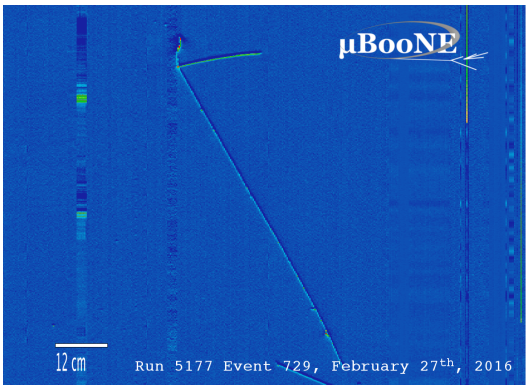

(e) Induction plane (V)

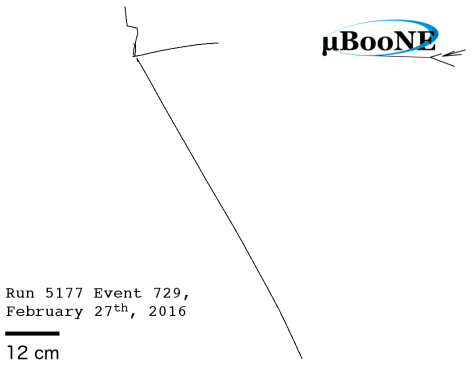

(f) Reconstructed 3D image (V plane projection)

Figure 20: Event view for run 5177, event 729, selected by selection II. The plots on the left show the event view in all three wire planes. A large gap of unresponsive wires is present in the U plane (see 20c). The plots on the right show the three-dimensional reconstructed image projected onto each wire plane. Comparing the reconstructed tracks to the wire plane views on the left it can be seen that the reconstruction successfully bridges gaps of unresponsive wires. The track reconstruction algorithm shown is pandoraNuPMA. All figures have the same scale (indicated by the white bar in the bottom left) and aspect ratio.

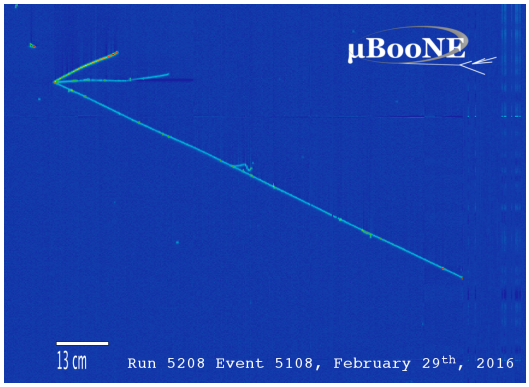

(a) Collection plane (Y)

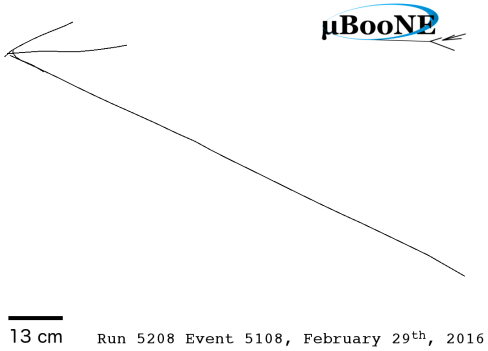

(b) 3Reconstructed 3D image (Y plane projection)

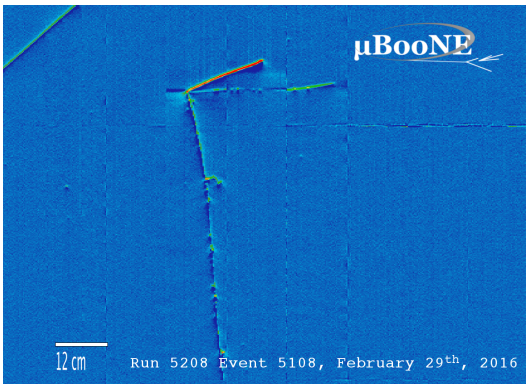

(c) Induction plane (U)

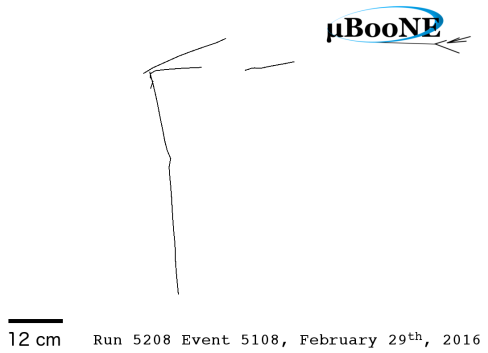

(d) Reconstructed 3D image (U plane projection)

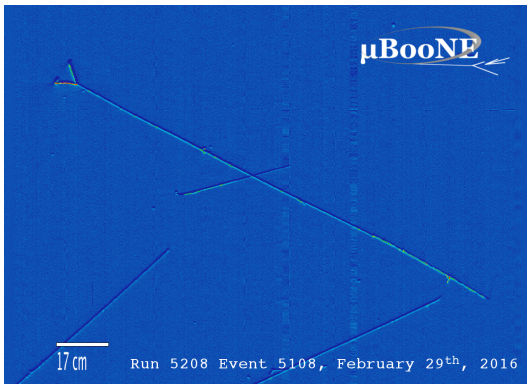

(e) Induction plane (V)

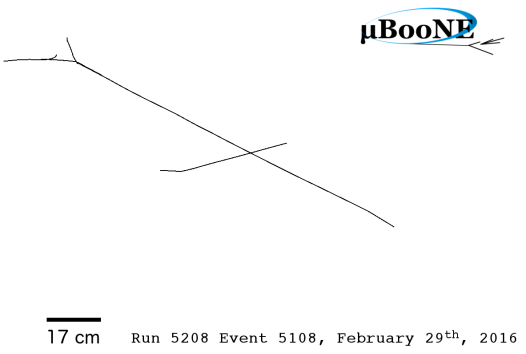

(f) Reconstructed 3D image (V plane projection)

Figure 21: Event view for run 5208, event 5108, selected by selection II. The plots on the left show the event view in all three wire planes. The plots on the right show the three-dimensional reconstructed image projected onto each wire plane. The track reconstruction algorithm shown is pandoraNuPMA. Note that some tracks visible on the left hand plots are missing on the right because they have been rejected in the cosmic removal pass. All figures have the same scale (indicated by the white bar in the bottom left) and aspect ratio.

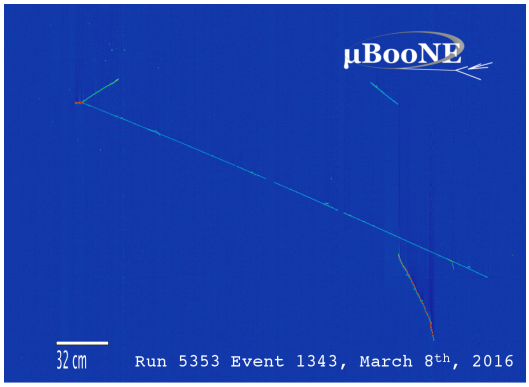

(a) Collection plane (Y)

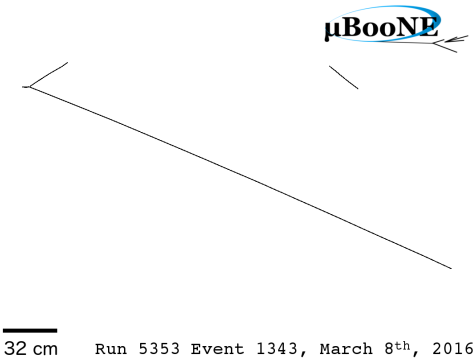

(b) Reconstructed 3D image (Y plane projection)

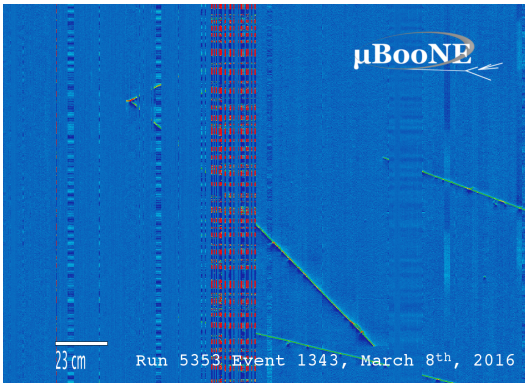

(c) Induction plane (U)

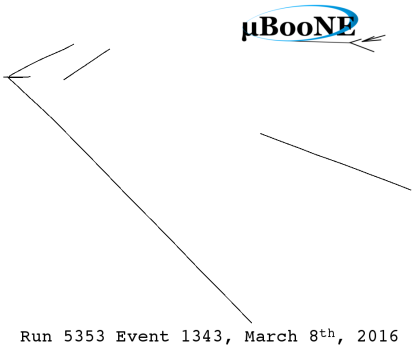

(d) Reconstructed 3D image (U plane projection)

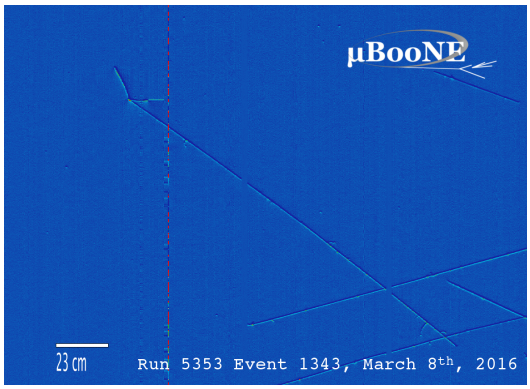

(e) Induction plane (V)

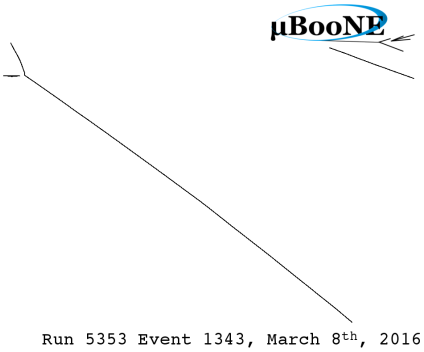

(f) Reconstructed 3D image (V plane projection)

Figure 22: Event view for run 5353, event 1353, selected by selection II. The plots on the left show the event view in all three wire planes. The U plane shows features of gaps of unresponsive wires and noise (vertical red stripes, see 22c). The plots on the right show the three-dimensional reconstructed image projected onto each wire plane. Comparing the reconstructed tracks to the wire plane views on the left it can be seen that the reconstruction successfully bridges gaps of unresponsive wires. The track reconstruction algorithm shown is pandoraNuPMA. Note that some tracks visible on the left hand plots are missing on the right because they have been rejected in the cosmic removal pass. All figures have the same scale (indicated by the white bar in the bottom left) and aspect ratio.

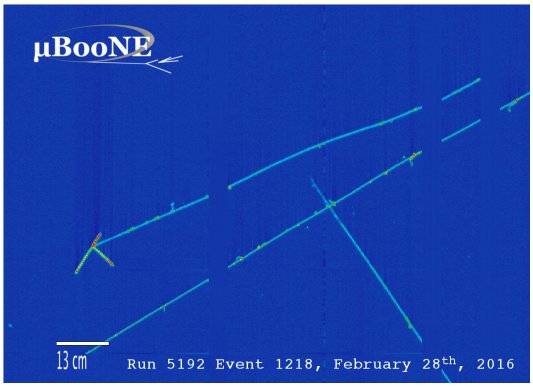

(a) Collection plane (Y)

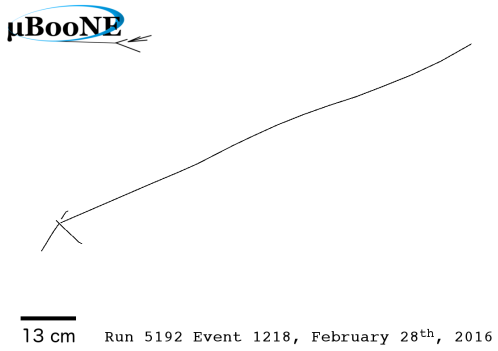

(b) Reconstructed 3D image (Y plane projection)

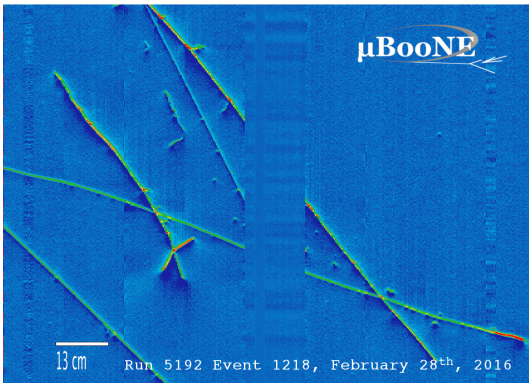

(c) Induction plane (U)

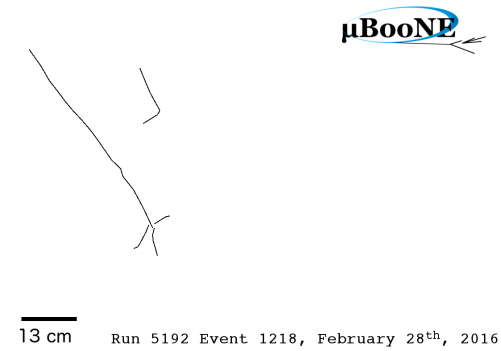

(d) Reconstructed 3D image (U plane projection)

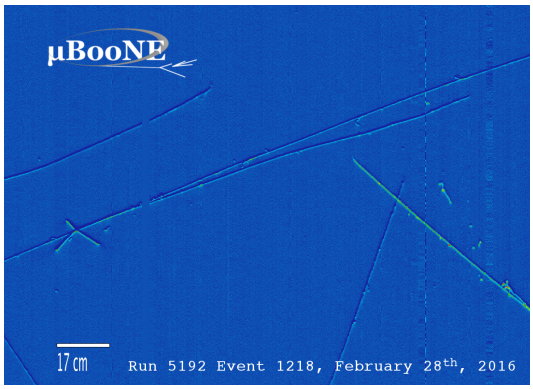

(e) Induction plane (V)

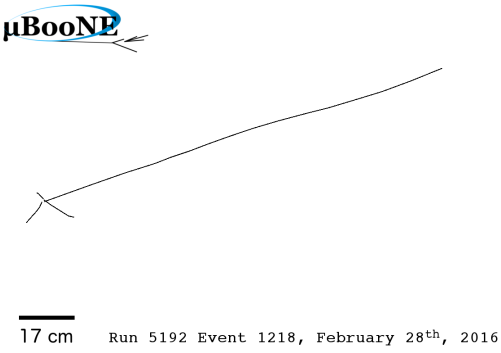

(f) Reconstructed 3D image (V plane projection)

Figure 23: Event view for run 5192, event 1218, selected by selection II. The plots on the left show the event view in all three wire planes. The U plane as well as the Y plane show gaps of unresponsive wires (see 23a and 23c). The plots on the right show the three-dimensional reconstructed image projected onto each wire plane. The track reconstruction algorithm shown is pandoraNuPMA. Note that some tracks visible on the left hand plots are missing on the right because they have been rejected in the cosmic removal pass. All figures have the same scale (indicated by the white bar in the bottom left) and aspect ratio.

6 Systematics and model variations

The understanding of systematic uncertainties on the previously shown kinematic distributions and for future cross section measurements is required for a physical interpretation of these results. Systematic uncertainties in MicroBooNE have not yet been fully addressed, but studies are ongoing and this Section discusses the sources of systematic uncertainties expected on these measurements together with some preliminary evaluations of some of the parameters.

The largest systematic uncertainty on a measurement of this kind is the uncertainty on the BNB flux. MicroBooNE's work on understanding beam flux uncertainties are largely based on the MiniBooNE studies [20]. The total uncertainty on the ν_μ BNB flux in the relevant energy range of this study is between 8% and 10%. This is already larger than the statistical uncertainty for a total flux integrated cross section measurement that could be derived from these data samples assuming a statistics of about 3000 observed events (see Tables 1 and 2). However, beam systematics and statistical uncertainties are currently of similar order in single differential distributions as shown in Section 4.3.

A large class of systematic uncertainties are detector parameters whose impact on the measurement through mis-modeling in the simulation or limited calibration precision needs to be studied. This starts – as described in Section 3.2.2 – with the understanding of noise in the detector, its correct modeling in the simulation, and a study of its impact on high-level reconstruction parameters such as tracking and vertexing. Similar efforts have to be taken for an improved understanding of the light modeling, propagation, and response, which impact the trigger and cut efficiencies of this analysis. Such studies are currently ongoing. The main detector parameters relevant at this stage are the determination of the electron lifetime, which relates to the argon purity, and the space charge effect. Low lifetimes lead to a higher absorption of ionization drift electrons in the detector. This can lead to hits on the TPC wires falling below reconstruction threshold and will have impact on the calorimetric reconstruction as well as the tracking efficiency. The effect won't be isotropic across the TPC volume, but will be stronger for ionization electrons produced near the cathode which must travel further to reach the anode plane. Data driven lifetime measurements using cosmic muons are currently being developed. The other effect that requires better understanding and modeling is the effect of space charge distorting the drift field and therefore the reconstructed track trajectories. The studies of data and MC comparisons [18] shows discrepancies in distributions of track start and end points between data and MC in the very top and very bottom of the detector. This indicates the presence of space charge accumulation. Since this effect seems to be concentrated at the edges of the active volume, the selections in this note use a smaller fiducial volume for the Y-direction, which is 20 cm from the edge of the active volume.

The last category of uncertainties are neutrino interaction model uncertainties. The model assumptions that enter a cross section measurement can impact the final result in two places - the estimation of background contamination and the estimation of the efficiency for signal interactions. As well as this, we would like to be able to compare our data to different models and possibly attempt to extract model parameters. All of this requires a framework for simulating various interaction models, and re-weighting model parameters through GENIE in LArSoft. This framework has been set up and is used in this section to demonstrate how it can be used to study model differences in MicroBooNE cross section channels. Here we use the above described selections for the ν_μ CC channel as an example.

The ν_μ CC inclusive channel is not the channel most sensitive to a lot of the nuclear effects and model differences, but it is expected to be the first cross section measurement to come out of MicroBooNE and has therefore been chosen for a first study. The following parameters or models have been picked for illustrations in this note:

- Axial vector mass for quasi-elastic interactions: At high neutrino energies a Relativistic

Fermi Gas (RFG) model of the nucleus, and a dipole axial form factor with axial mass of approximately 1 GeV, was found to agree well with data. In observations of CCQE events at MiniBooNE [21], this model was found to not agree well with the data, and fits resulted in an "effective" axial mass value of 1.35 GeV. Here we modify the axial vector mass from the GENIE baseline value of $M_A = 0.99$ GeV to $M_A = 1.35$ GeV by re-weighting the GENIE baseline simulation [22]. The primary effect of the axial mass increase is an increase in normalisation. The effect on the total number of expected selected events is of the order of 24%.

- Meson exchange currents (MEC): Rather than introducing an effective parameter, additional processes are proposed which would address the discrepancies seen in the MiniBooNE data. MEC are one way to model an additional process, where a neutrino interacts with a correlated pair of nucleons (which may be in a quasi-deuteron state). It is also often referred to as 2p2h, or multinucleon interactions. As the correlation between nucleons is mediated by the exchange of a meson, this process is known as MEC. The model referred to as MEC in the following plots is a microscopic model for MEC by Nieves *et al.* [23]. The effect on the total number of expected selected events is of the order of 24%.

- Effective spectral functions with transverse enhancement: The Transverse Enhancement Model (TEM) [24] is another way to model the nuclear effects. In this model, the transverse cross-section is enhanced based on the observation in the electron scattering data. The empirical superscaling function is modeled with the effective spectral function (ESF) [25]. The ESF replaces the RFG model which is used in all other samples as the GENIE default. Only the lepton is effected by this - there is no impact on the hadronic side of the interaction. The effect on the total number of expected selected events is of the order of 13%.

The effect of varying M_A on the plain ν_μ CC true muon momentum distributions before any event selection is shown in Figure 24. The effect on the distributions after selection for both, selection I and II, presented in this note, is shown in Figure 25. The same study for the MEC and TEM models is shown in Figure 26.

The final MicroBooNE data sample should have the statistical power to observe these model differences and add insights on the viability of the models.

For a future cross section measurement, model uncertainties enter through the efficiency and background predictions. The backgrounds in this selection are relatively small, and the efficiency is not strongly impacted by these model variations. For these reasons, the impact of model uncertainties on a final cross section measurement is rather small compared to current statistical errors. This study will be extended as we move forward towards cross section measurements and different interaction channels.

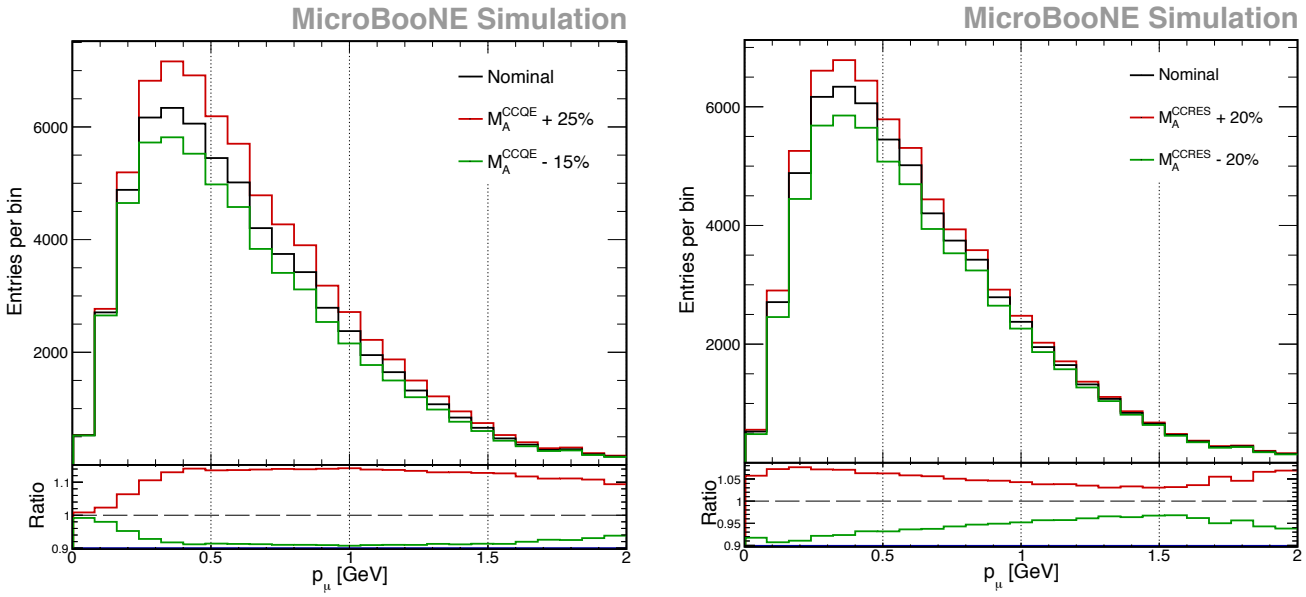

(a) Axial mass for CC quasi-elastic.

(b) Axial mass for CC resonance neutrino production.

Figure 24: The black distributions show the number of events as a function of the true muon momentum for nominal values of GENIE parameters before any event selection. The red and green distributions show the number of events with the axial mass for CC quasi-elastic, 24a, and CC resonance interaction, 24b, changed by + and -1σ respectively. In GENIE, M_A is given with a fractional uncertainty of $^{+25\%}_{-15\%}$ for quasi-elastic interactions and $\pm 20\%$ for resonance production interactions, [22].

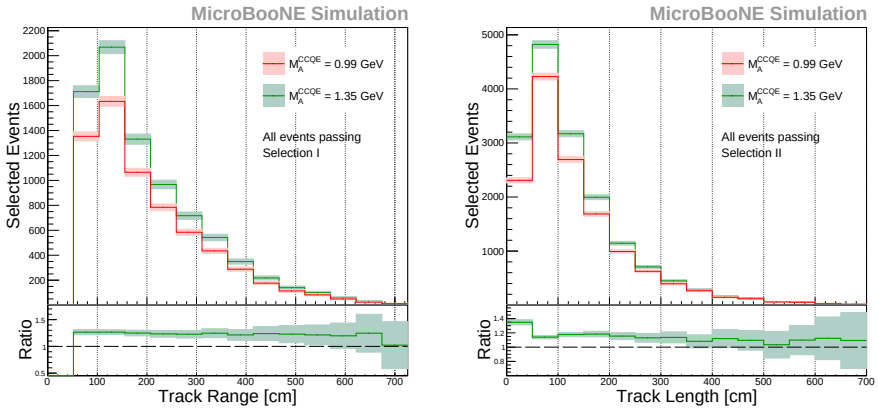

(a) Selection I: track range.

(b) Selection II: track length.

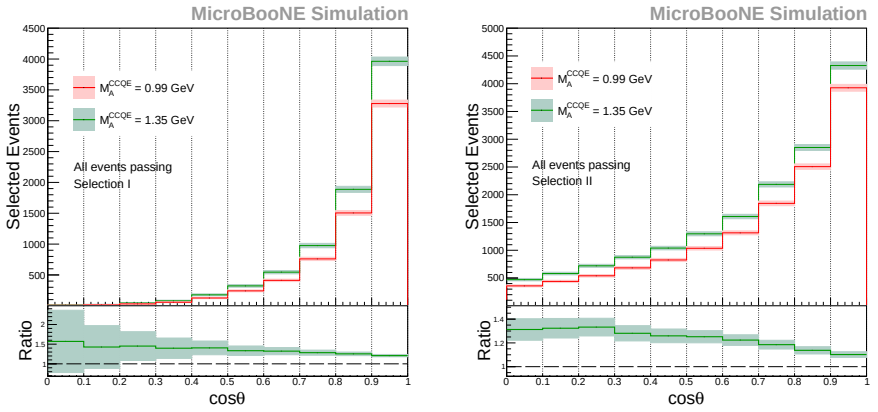

(c) Selection I: $\cos(\theta)$.

(d) Selection II: $\cos(\theta)$.

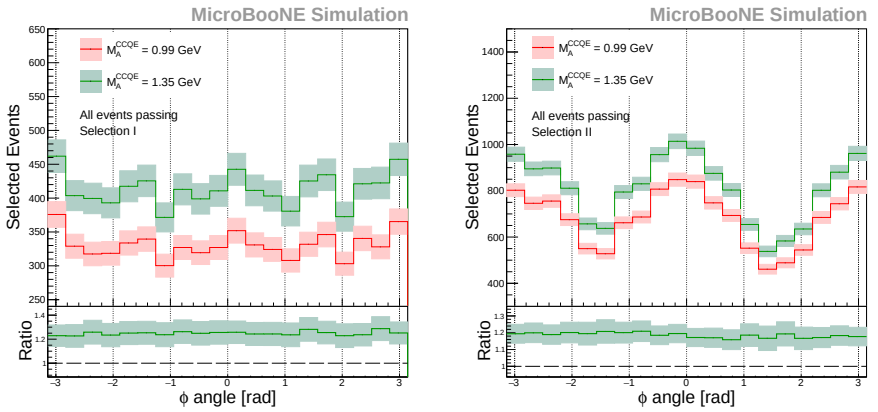

(e) Selection I: ϕ.

(f) Selection II: ϕ.

Figure 25: The effect of re-weighting the axial vector mass for quasi-elastic processes on the expected muon reconstructed kinematic distributions for selection I (left) and selection II (right). The red distribution shows the baseline simulation of BNB+Cosmic events, using $M_A = 0.99$ GeV. The green curve shows the expected distribution using $M_A = 1.35$ GeV, as motivated by the MiniBooNE measurements [21]. The sum of all selected events including ν_μ CC signal as well as backgrounds is plotted as a function of reconstructed kinematics of the muon candidate track, which corresponds to the red histogram in Figures 12, 13, and 14). The shaded areas show the statistical uncertainty only. The plots are normalized to expected event numbers during a run period of roughly one year. The distributions of $\cos(\theta)$ are shown only for the range between 0 and 1 for better visibility.

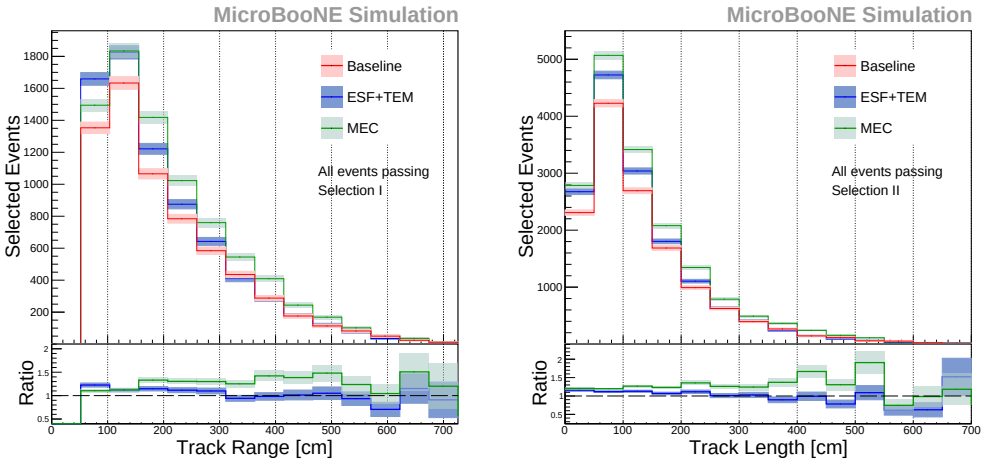

(a) Selection I: track range.

(b) Selection II: track length.

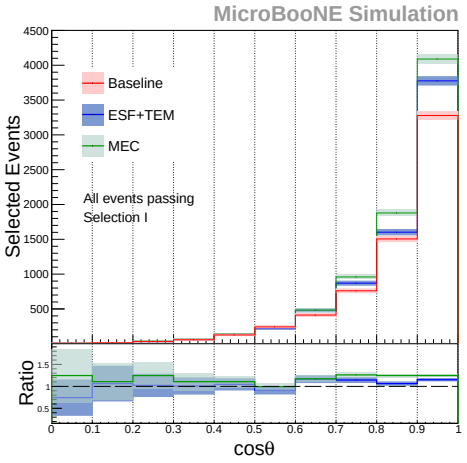

(c) Selection I: $\cos(\theta)$.

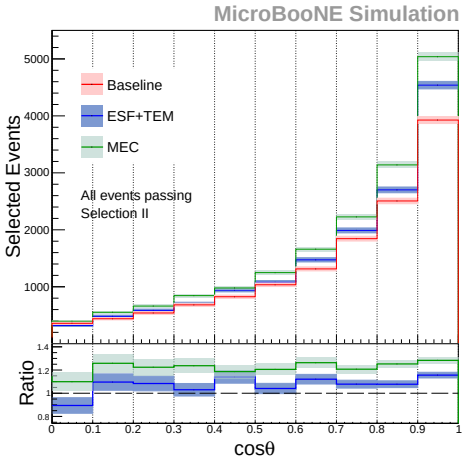

(d) Selection II: $\cos(\theta)$.

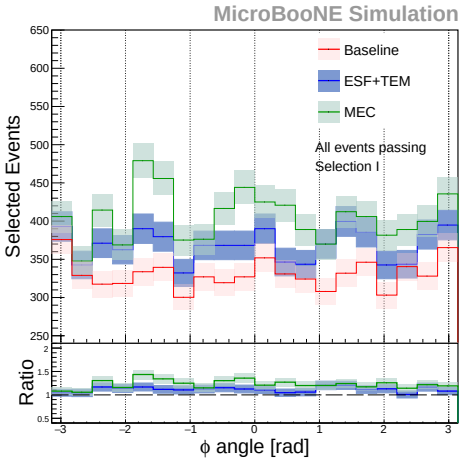

(e) Selection I: ϕ.

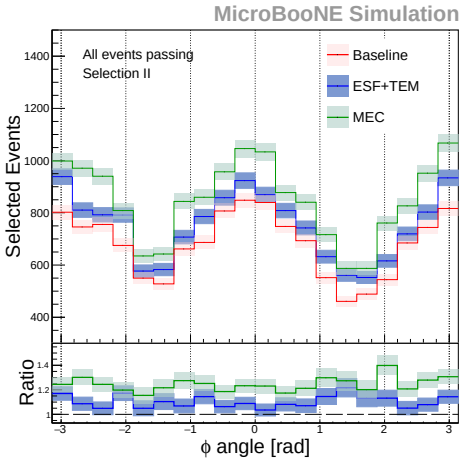

(f) Selection II: ϕ.

Figure 26: The effect of using different nuclear models in the neutrino simulation on the expected muon reconstructed kinematic distributions for selection I (left) and selection II (right). Green distribution shows the effect of simulating Meson Exchange Current (MEC) interactions in addition to the GENIE nominal ones (CC, RES, DIS, etc.). The blue distribution shows the effect of using the Effective Spectral Function model (in place of the GENIE nominal Bodek-Ritchie Fermi Gas model) and the Transverse Enhancement model (which is a simplified version of MEC). The sum of all selected events including ν_μ CC signal as well as backgrounds is plotted as a function of reconstructed kinematics of the muon candidate track, which corresponds to the read histogram in Figures 12, 13, and 14). The shaded areas show the statistical uncertainty only. The plots are normalized to expected event numbers during a run period of roughly one year. The distributions of $\cos(\theta)$ are shown only for the range between 0 and 1 for better visibility.

7 Summary and Outlook

The study presented here demonstrates that with MicroBooNE we are able to successfully select neutrino interactions in a LArTPC located on the surface. This is imposingly proven by comparing the selected events in the on-beam and off-beam stream listed in Tables 1 and 2. The reconstruction and selection of events is done in a fully automated way. The muon kinematic distributions presented in Section 4.3 show that the off-beam subtracted data events follow the expectation from the simulation of neutrino interactions in MicroBooNE. The path towards a first measurement of the ν_μ CC inclusive cross section in MicroBooNE now requires improved understanding and implementation of the current operating conditions of the MicroBooNE detector, such as the noise sources, their simulation and removal techniques. A major step to better agreement between data and simulation is the replacement of cosmic background obtained here from CORSIKA simulations by overlays of off-beam data. Several ideas also exist that increase the selection efficiency: Besides improvements to hit reconstruction, clustering and tracking algorithms, major improvements are expected from a more sophisticated flash-track matching approach, which would more reliably detect cosmic tracks as being out of time with the beam arrival. During the 2016 summer beam shutdown period, MicroBooNE is going to install a cosmic ray tagger system, which will likely improve cosmic tagging for data taken in the future. Section 6 mentioned that studies to address systematic uncertainties have been started.

Over the coming months, the work presented here will move forward towards a first ν_μ CC inclusive cross section measurement in MicroBooNE. With about five times the statistics used in this note already available and anticipated improvements in selection efficiencies, MicroBooNE will perform interesting physics measurements.

References

[1] The MicroBooNE Collaboration. MicroBooNE. *to be published*, 2016.

[2] The MicroBooNE Collaboration. Measurement of the Average Drift Velocity Utilizing UV Laser Data. *MicroBooNE Public Note*, MICROBOONE-NOTE-1009-PUB, 2016. URL `http://www-microboone.fnal.gov/publications/publicnotes/`.

[3] The MicroBooNE Collaboration. Cosmic Shielding Studies at MicroBooNE. *MicroBooNE Public Note*, MICROBOONE-NOTE-1002-PUB, 2016. URL `http://www-microboone.fnal.gov/publications/publicnotes/`.

[4] The MicroBooNE Collaboration. First neutrino interactions observed with the MicroBooNE Liquid-Argon TPC detector. *MicroBooNE Public Note*, MICROBOONE-NOTE-1005-PUB, 2015. URL `http://www-microboone.fnal.gov/publications/publicnotes/`.

[5] The MicroBooNE Collaboration. Noise Characterization and Filtering in the MicroBooNE TPC. *MicroBooNE Public Note*, MICROBOONE-NOTE-1016-PUB, 2016. URL `http://www-microboone.fnal.gov/publications/publicnotes/`.

[6] The MicroBooNE Collaboration. A Method to Extract the Charge Distribution Arriving at the TPC Wire Planes in MicroBooNE. *MicroBooNE Public Note*, MICROBOONE-NOTE-1017-PUB, 2016. URL `http://www-microboone.fnal.gov/publications/publicnotes/`.

[7] The MicroBooNE Collaboration. The Pandora multi-algorithm approach to automated pattern recognition in LAr TPC detectors. *MicroBooNE Public Note*, MICROBOONE-NOTE-1015-PUB, 2016. URL `http://www-microboone.fnal.gov/publications/publicnotes/`.

[8] The MicroBooNE Collaboration. MC performance study for an early ν_μ charged-current inclusive analysis with MicroBooNE. *MicroBooNE Public Note*, MICROBOONE-NOTE-1004-PUB, 2015. URL `http://www-microboone.fnal.gov/publications/publicnotes/`.

[9] The MicroBooNE Collaboration. Reconstruction of $\pi^0 \to \gamma\gamma$ decays from muon neutrino charged current interactions in data. *MicroBooNE Public Note*, MICROBOONE-NOTE-1012-PUB, 2016. URL `http://www-microboone.fnal.gov/publications/publicnotes/`.

[10] The MicroBooNE Collaboration. MicroBooNE Detector Stability Over Time. *MicroBooNE Public Note*, MICROBOONE-NOTE-1013-PUB, 2016. URL `http://www-microboone.fnal.gov/publications/publicnotes/`.

[11] T. Kobilarcik and T. Miceli and Z. Pavlovic. BNB Protons on Target for MicroBooNE. *MicroBooNE Internal Note*, DocDB 5719, 2016.

[12] E. D. Church. Larsoft: A software package for liquid argon time projection drift chambers. *arXiv:1311.6774*, 2016.

[13] C. Andreopoulos et al. The GENIE Neutrino Monte Carlo Generator. *Nucl. Instrum. Meth.*, A614:87–104, 2010. doi: 10.1016/j.nima.2009.12.009.

[14] Corsika: A monte carlo code to simulate extensive air showers. *Forschungszentrum Karlsruhe Report FZKA*, 1998. URL `https://www.ikp.kit.edu/corsika/70.php`.

[15] S. Agostinelli et al. Geant4—a simulation toolkit. *NIM A*, 506(3):250 – 303, 2003. URL `http://www.sciencedirect.com/science/article/pii/S0168900203013688`.

[16] The ArgoNeuT Collaboration (R. Acciarri (Fermilab) et al.). A study of electron recombination using highly ionizing particles in the argoneut liquid argon tpc. *JINST*, 8, 2013. URL `http://arxiv.org/pdf/1306.1712.pdf`.

[17] M. Antonello et al. *Adv. High Energy Phys.*, 260820, 2013. URL `https://inspirehep.net/search?p=find+eprint+1210.5089`.

[18] The MicroBooNE Collaboration. A Comparison of Monte-Carlo Simulations and Data from MicroBooNE. *MicroBooNE Public Note*, MICROBOONE-NOTE-1014-PUB, 2016. URL `http://www-microboone.fnal.gov/publications/publicnotes/`.

[19] The MicroBooNE Collaboration. Michel Electron Reconstruction Using the MicroBooNE LArTPC Cosmic Data. *MicroBooNE Public Note*, MICROBOONE-NOTE-1014-PUB, 2016. URL `http://www-microboone.fnal.gov/publications/publicnotes/`.

[20] The MiniBooNE Collaboration. Neutrino flux prediction at miniboone. *Phys. Rev. D*, 79:072002, 2009.

[21] A. A. Aguilar-Arevalo, et al. First measurement of the muon neutrino charged current quasielastic double differential cross section. *Phys. Rev. D*, 81:092005, May 2010. doi: 10.1103/PhysRevD.81.092005. URL `http://link.aps.org/doi/10.1103/PhysRevD.81.092005`.

[22] Costas Andreopoulos, Christopher Barry, Steve Dytman, Hugh Gallagher, Tomasz Golan, Robert Hatcher, Gabriel Perdue, and Julia Yarba. The GENIE Neutrino Monte Carlo Generator: Physics and User Manual. 2015.

[23] J. Nieves, I. Ruiz Simo, and M. J. Vicente Vacas. Inclusive charged-current neutrino-nucleus reactions. *Phys. Rev. C*, 83:045501, Apr 2011. doi: 10.1103/PhysRevC.83.045501. URL `http://link.aps.org/doi/10.1103/PhysRevC.83.045501`.

[24] A. Bodek, H. S. Budd, and M. E. Christy. Neutrino quasielastic scattering on nuclear targets. *EPJ C*, 71(9):1726, 2011. ISSN 1434-6044. doi: 10.1140/epjc/s10052-011-1726-y. URL http://dx.doi.org/10.1140/epjc/s10052-011-1726-y.

[25] A. Bodek, M. E. Christy, and B. Coopersmith. Effective spectral function for quasielastic scattering on nuclei. *The European Physical Journal C*, 74(10):1–17, 2014. ISSN 1434-6052. doi: 10.1140/epjc/s10052-014-3091-0. URL http://dx.doi.org/10.1140/epjc/s10052-014-3091-0.